nature nanotechnology

SUPPLEMENTARY INFORMATION

DOI: 10.1038/NNANO.2015.259

# High-speed DNA-based rolling motors powered by RNase H

Kevin Yehl[†], Andrew Mugler[‡§], Skanda Vivek[‡], Yang Liu[†], Yun Zhang[†], Mengzhen Fan[†], Eric R. Weeks[‡], Khalid Salaita[†*]

**Supplementary Table 1: Oligonucleotide sequences**

| ID | Sequence (5'-3') |
|---|---|
| DNA Anchor | /5AmMC6/GAGAGAGATGGGTGCTTTTTTTTTTTTTTT/3ThiolMC3-D/ |
| RNA/DNA Chimera Substrate | GCACCCATCTCTCTCrCrCrCrCrCrCrUrGrUrGrArUrUrGrArUrUrArCrU /3Cy3Sp/ |
| DNA Control Substrate | GCACCCATCTCTCTCCCCCCCTGTGATTGATTACT/3Cy3Sp/ |
| Particle DNA | /5Hexynyl/TTTTTTTTTTTTTTTTAGTAATCAATCACAG |
| RNA Complement | TTTTTTTTTTTTTTTTAGTAATCAATCACAG |
| Particle Blocking Strand | CTGTGATTGATTACT |
| Perfect Match | /5Hexynyl/TTTTTTTTTTTTTTTTmAmGTAAT**C**AAmUmC |
| SNP | /5Hexynyl/TTTTTTTTTTTTTTTTmAmGTAAT**T**AAmUmC |

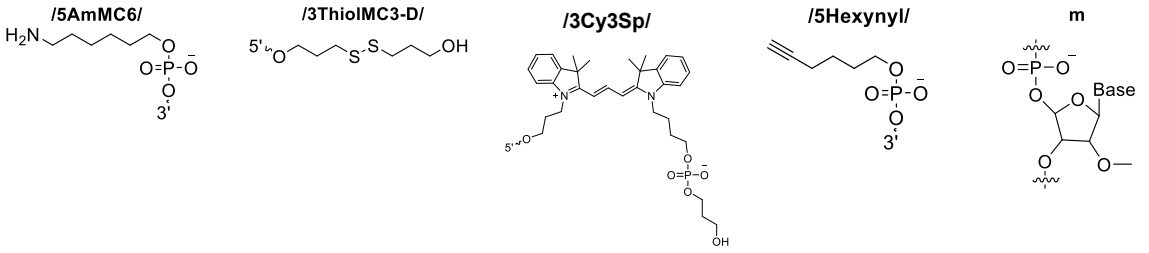


**Supplementary Table 1.** Table summarizing the sequences of oligonucleotides and their naming system. The sequences are displayed in a 5' to 3' orientation, the red text indicates RNA bases, and the underlined bases represent the RNase H recognition sequence. The 3' and 5' DNA and RNA modifications indicated in the table are illustrated below it.

DOI: 10.1038/NNANO.2015.259

**Supplementary Figure 1: RNA surface hybridization kinetics**

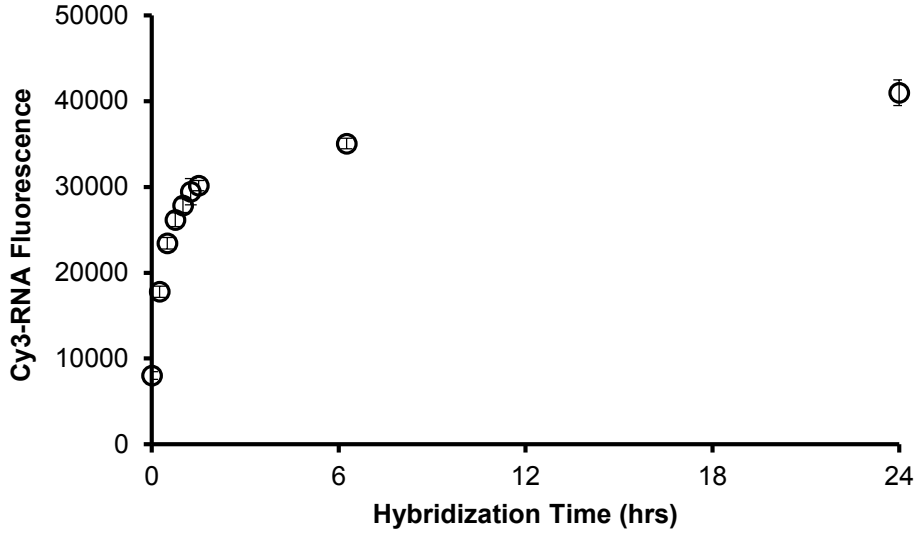


**Supplementary Figure 1.** A representative kinetic plot of hybridization between 3'Cy3-RNA (100 nM) and surface immobilised DNA anchor strand in 1x PBS. Error bars represent the standard deviation in the average fluorescence intensity from at least 5 regions across each channel. An increase in fluorescence intensity is indicative of an increase in the surface density of RNA that is due to greater hybridization. Near saturation is typically observed after ~6 hrs of hybridization.

**Supplementary Figure 2: Determining RNA surface density**

RNA surface density was controlled by varying the concentration of RNA during hybridization with the surface immobilised anchor strand (10-500 nM). RNA density was then quantified by releasing the immobilised 3'Cy3-RNA from the surface by addition of 1 µg RNase A and measuring the resulting fluorescence with the optical microscope. The amount of RNA released was quantified using a fluorescence calibration curve by measuring the fluorescence intensity of known concentrations of Cy3-RNA under identical conditions. The amount of released RNA was then divided by the surface area of the IBIDI channel (79.7 $mm^2$) to determine the average RNA surface density in units of molecules/$\mu m^2$.

**a**

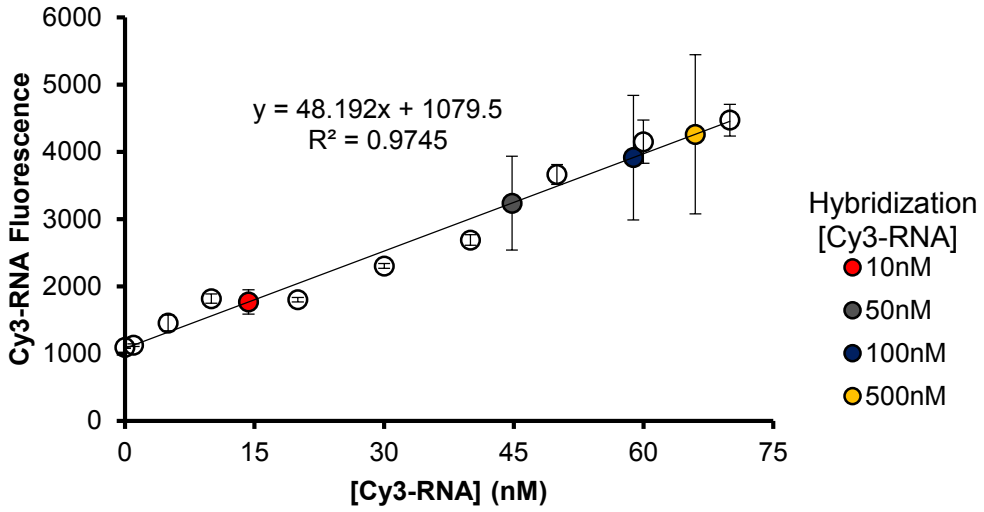


**b**

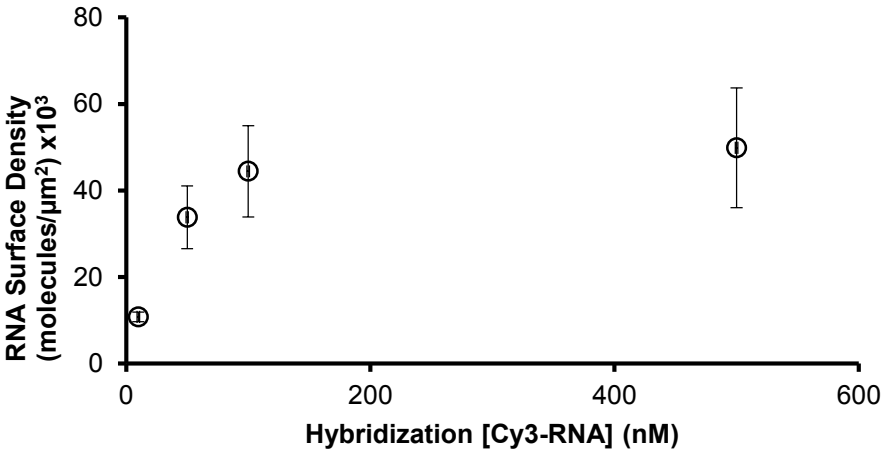


**Supplementary Figure 2. a**, Fluorescence calibration curve for 3'Cy3-RNA measured using a fluorescence microscope (white circles). This calibration curve was fit using least squares regression analysis. The calibration curve was then used to quantify the concentration of released RNA from surfaces following RNase A treatment. This measurement was repeated for hybridization concentrations of 10 (red circle), 50 (green circle), 100 (blue circle), and 500 (yellow circle) nM RNA. The data in **a** were normalised by the substrate surface area and plotted in **b** to display the average RNA density per $\mu m^2$ as a function of RNA hybridization concentration. Note that the RNA surface density saturates upon hybridization with concentrations of 100 nM or greater.

DOI: 10.1038/NNANO.2015.259

**Supplementary Figure 3: RNA monolayer stability towards dithiothreitol (DTT) displacement**

DTT is a dithiol reducing agent that will prolong RNase H stability; however, DTT will also degrade the RNA monolayer surface through thiol displacement. To balance these two parameters, the maximum DTT concentration that did not lead to significant RNA exchange was determined by incubating RNA substrates in DTT solutions of varying concentrations in 1xPBS (see below). We found that a 10 μm DTT concentration did not lead to detectable loss of surface bound 3' Cy3-RNA after a 4 hour incubation.

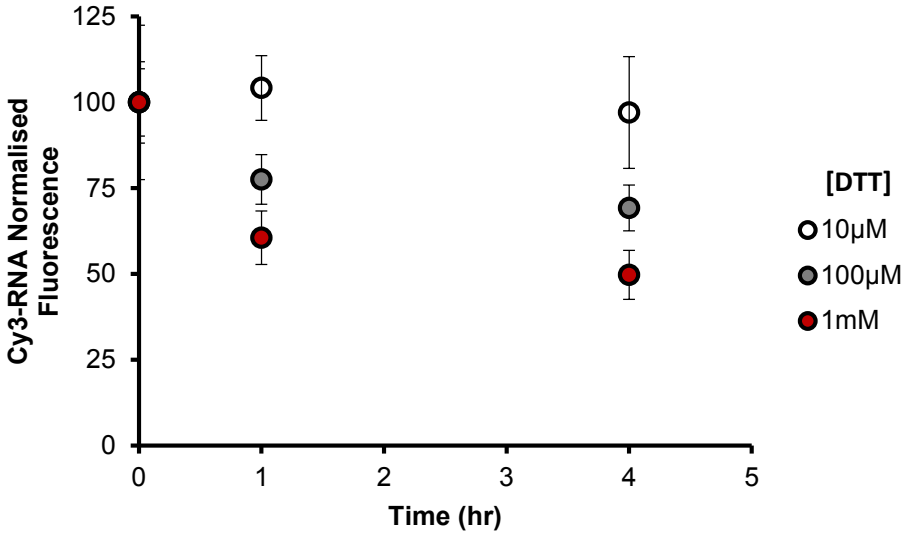


**Supplementary Figure 3.** A kinetic plot showing the 3' Cy3-RNA fluorescence intensity as a function of DTT incubation time at concentrations of 10 μM (white), 100 μM (gray), and 1 mM (red) in 1xPBS. Error bars represent the standard deviation across at least 5 different regions from each micro-channel. Based on this analysis, we found that a 1 mM DTT solution led to ~50% loss of RNA after 4 hrs. Surfaces were stable for weeks in the absence of DTT in PBS.

**Supplementary Figure 4: Passivation to maintain RNase H activity**
Initially, when measuring the hydrolysis of surface immobilised RNA-DNA duplexes, we found that RNase H was completely inhibited. Since RNase H contains multiple cysteine residues, we first suspected that enzyme inhibition was due to irreversible binding of the enzyme to the Au surface. To prevent nonspecific binding, the Au surface was passivated with $SH(CH_2)_{11}(OCH_2CH_2)_6OCH_3$ (SH-PEG) because PEG is known to greatly reduce nonspecific interactions with surfaces (**Supplementary Fig. 4a**). To test the assumption that RNase H inhibition was due to Au film binding, the DNA monolayer surface was backfilled with SH-PEG under a range of conditions, where the SH-PEG concentration and the passivation time were varied. It was determined that complete surface passivation occurred after 4 hrs of incubation with a 100 μM SH-PEG solution. This was inferred by observing a saturation in the loss of fluorescence of FAM labeled DNA anchor strand (**Supplementary Fig. 4b**). Next, RNase H hydrolysis of surface immobilised RNA duplexed with DNA was investigated under the various passivation conditions by measuring the loss in fluorescence of Cy3 labeled RNA throughout the channel over time (**Supplementary Fig. 4c-f**). When the channel was SH-PEG passivated for shorter durations (2 hrs), we observed that the fluorescence intensity varied significantly across the length of the well; regions near the port where RNase H was added had the lowest intensities, while regions furthest away from this site showed minimal substrate hydrolysis (**Supplementary Fig. 4e top**). In contrast, channels that were blocked for 6 hrs showed homogeneous fluorescence intensities indicating uniform RNase H activity levels (**Supplementary Fig. 4e bottom**). The variation in substrate hydrolysis as a function of passivation time is shown in **Supplementary Fig. 4f**. All hydrolysis experiments were carried out under 25 mM Tris pH 8.0, 8 mM NaCl, 37.5 mM KCl, and 1.5 mM $MgCl_2$.

DOI: 10.1038/NNANO.2015.259

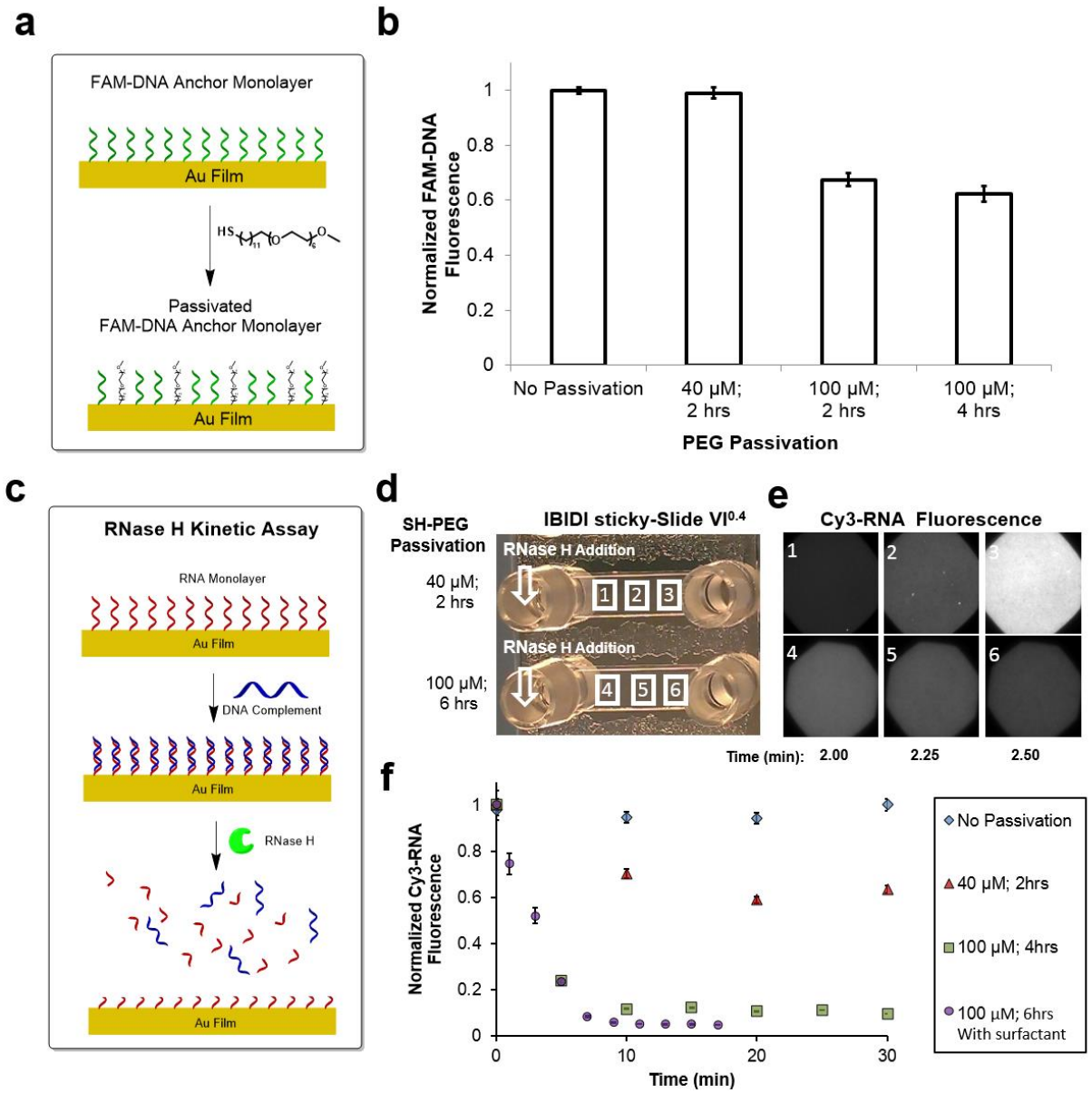


**Supplementary Figure 4. a**, Schematic showing surface passivation with a thiolated PEG. **b,** Bar graph summarizing the loss in fluorescence of the FAM labeled DNA anchor strand upon incubating the gold surface with SH-PEG under various concentrations and incubation times. Error bars represent the standard deviation of five fluorescence measurements across the length of the micro-channel. **c**, Schematic displaying the fluorescence assay used to measure RNase H activity. **d**, A photograph of the micro-channel array substrate used throughout the current work. Boxes indicated the location of where Cy3 fluorescence was measured in relation to the channel port where RNase H was introduced. **e**, Representative Cy3 fluorescence images collected at different positions along the micro-channel after ~2 min of RNase H addition for samples that were passivated for 2 hrs (top row) and 6 hours (bottom row). **f**, Kinetic plot showing the rate of RNA substrate hydrolysis as a function of passivation conditions. Note that 10% formamide and 0.75% Triton-X surfactant were included in the reaction buffer for the surface that was passivated under 100 μM SH-PEG for 6 hrs. Error bars represent the standard deviation of fluorescence intensity in a single image acquired at a specific position along the well.

**Supplementary Figure 5: RNase H kinetics for surface-bound RNA**

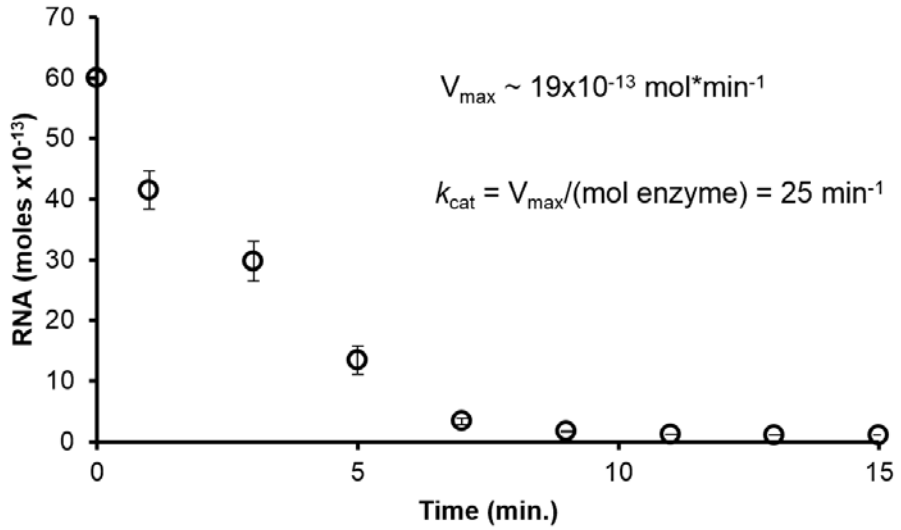


**Supplementary Figure 5.** A representative kinetic plot showing RNase H hydrolysis of surface immobilised RNA hybridised to a complementary DNA strand. The error bars represent the standard deviation in the average fluorescence intensity from at least 5 different regions across the micro-channel. The absolute number of RNA molecules (y-axis) was inferred by multiplying the area of the micro-channel by the density of RNA per μm$^2$ that was obtained from the calibration and RNA release measurements shown in **Supplementary Fig. 2**. $V_{max}$ was determined by measuring the initial rate of reaction between 0 and 1 min, and $k_{cat}$ was subsequently calculated by using this value of $V_{max}$ and dividing it by the concentration of the enzyme.

DOI: 10.1038/NNANO.2015.259

**Supplementary Figure 6: Determining DNA particle surface density**

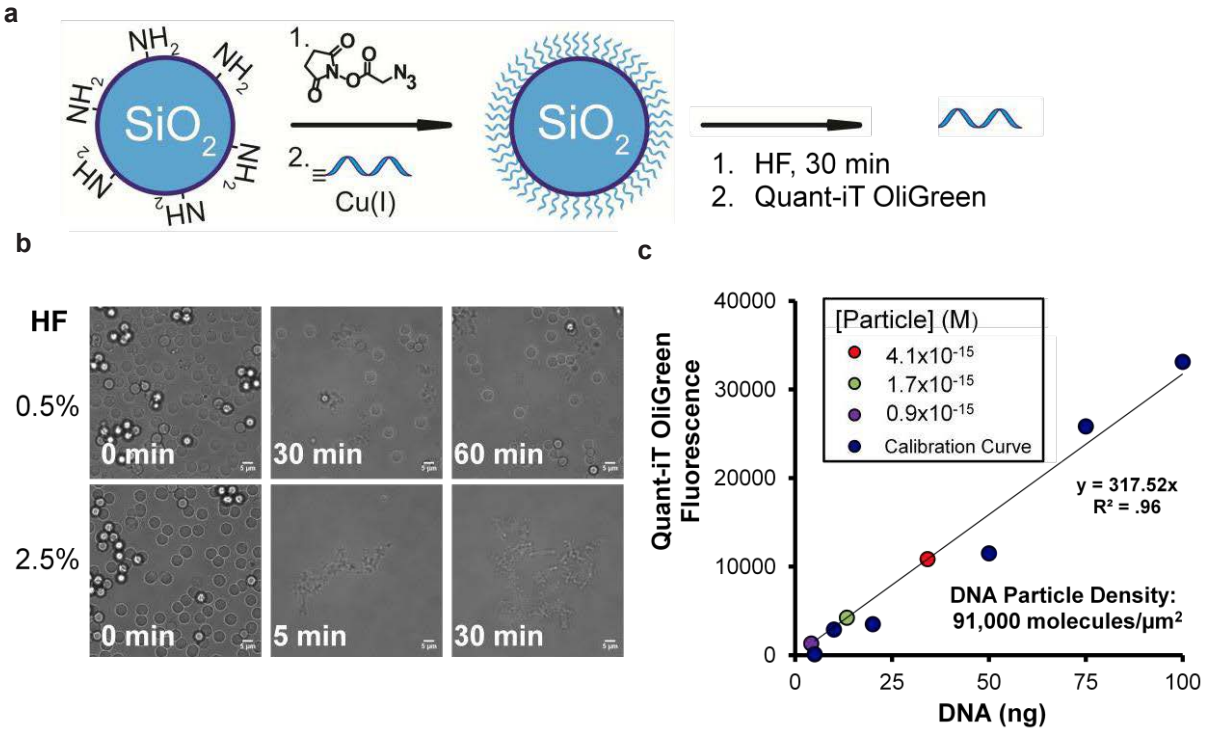


**Supplementary Figure 6. a,** Schematic showing the approach used to modify the particle with DNA and then to determine the DNA loading number. 5-μm aminated silica beads were functionalised with an N-hydroxysuccinimidyl azide heterobifunctional linker (see Methods). These particles were then coupled to a 5'-alkyne terminated DNA strand through Cu(I) catalysed Huisgen cyclo-addition. The DNA density on the particle was determined by releasing the DNA from the surface using HF etching and then quantifying the DNA concentration with a fluorescence assay. **b**, Brightfield images showing particle dissolution over time during incubations with 0.5% and 2.5% HF in 1x PBS. Based on brightfield imaging, spherical particles appeared to be completely etched after 30 min of incubation in 2.5% HF. **c**, Calibration curve for the 5'alkyne particle DNA using the Quant-iT OliGreen fluorescence assay. Note that the DNA used in this calibration was incubated in 2.5% HF under identical conditions to those used to etch the particles. The DNA released from etched microparticles of three different concentrations (red, $4.1 \times 10^{-15}$ M; green, $1.7 \times 10^{-15}$ M; and purple, $0.9 \times 10^{-15}$ M) from two independent syntheses was then quantified by using the Quant-iT assay. Based on these three, the average DNA density was ~91,000 molecules/μm$^2$ (footprint of 11 ±3 nm$^2$ per molecule). Thus, the DNA density matched that of the RNA density on the planar substrate and was sufficiently high to ensure a high degree of polyvalency (~$10^4$ contacts/μm$^2$), minimising motor detachment from the substrate which limits run processivity.

**Supplementary Figure 7: Particle motion on DNA and RNA surfaces**

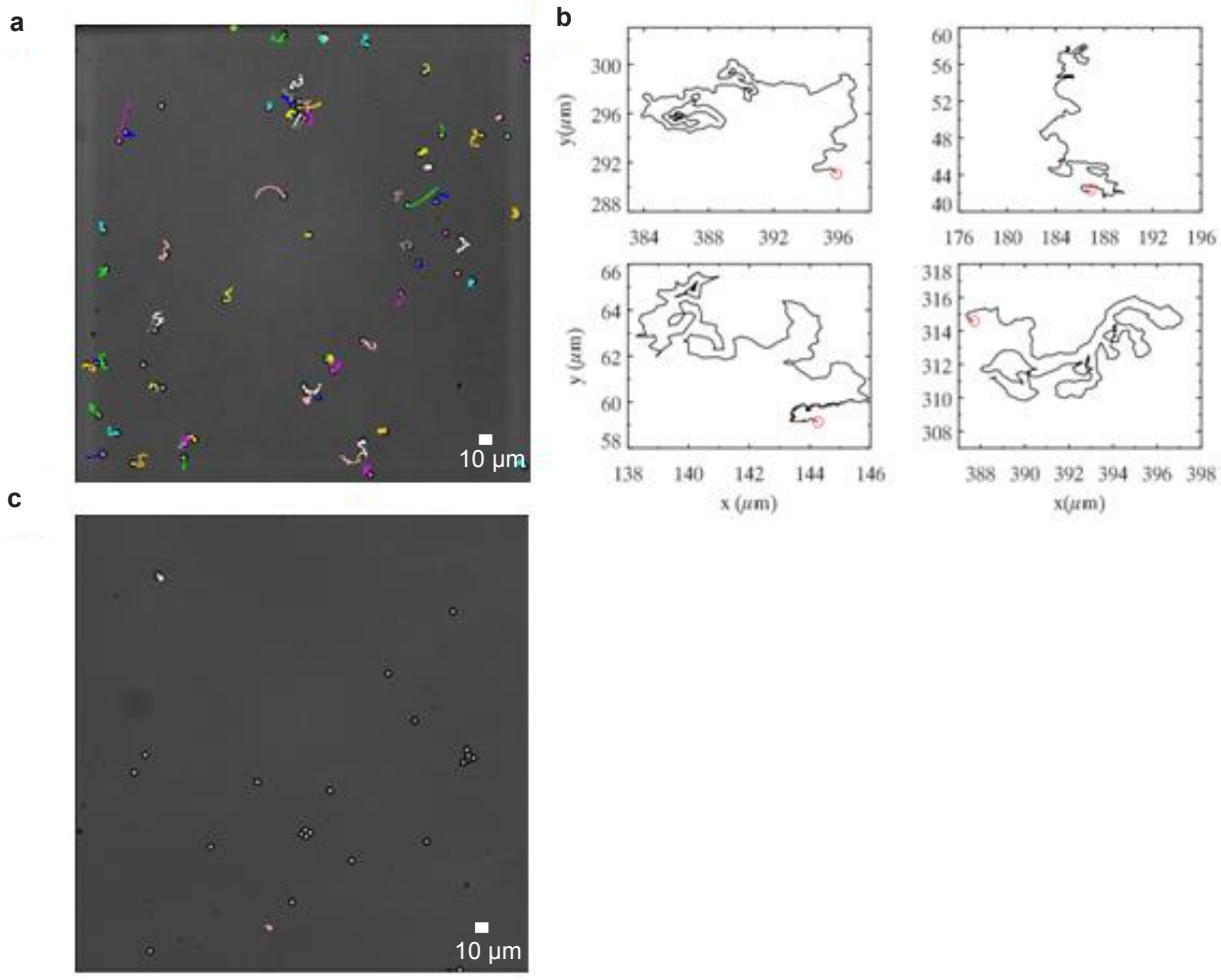


**Supplementary Figure 7. a**, Representative BF image superimposed with particle trajectories acquired over a 30 min duration following addition of RNase H. The timelapse was collected at 5 s intervals and shows that the majority (>90%) of particles moved following RNase H addition. The colours are randomly assigned to different particle trajectories. **b**, Representative zoomed in particle trajectories from **a** showing the self-avoiding diffusion of particles. **c**, Representative BF image superimposed with particle trajectories when the RNA substrate is replaced with a DNA substrate. Note that none of the particles moved following RNase H addition.

DOI: 10.1038/NNANO.2015.259

**Supplementary Figure 8: Widefield microscopy track width analysis**

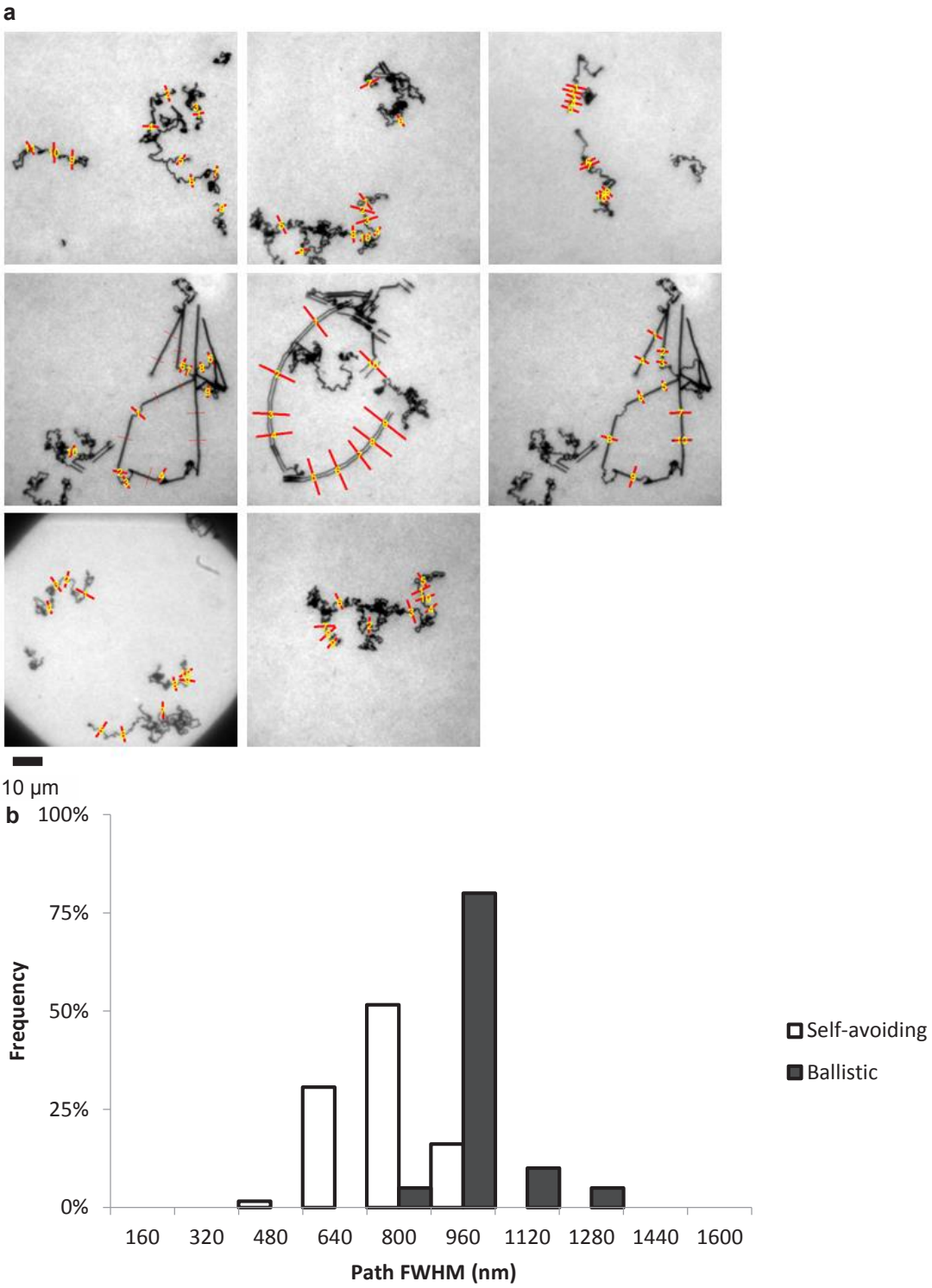


**Supplementary Figure 8. a**, Widefield microscopy images of Cy3 fluorescence depletion tracks obtained after incubating the RNA substrate with DNA-modified particles and RNase H for 30-60 min. The numbered line scans (red) represent the regions where line widths were determined and used for histogram analysis of average path width. **b**, Histogram analysis showing the full width

at half maxima of labeled line scans. As described in the main text, some particles toggled between linear (ballistic) and self-avoiding paths. We classified the tracks as ballistic and self-avoiding and then reported the distribution of these two categories in the histogram. The mean FWHM of ballistic tracks was 1.0 ±0.1 μm while the mean FWHM for self-avoiding tracks was 720 ±110 nm.

DOI: 10.1038/NNANO.2015.259

**Supplementary Figure 9: Structured illumination microscopy (SIM) track width analysis**

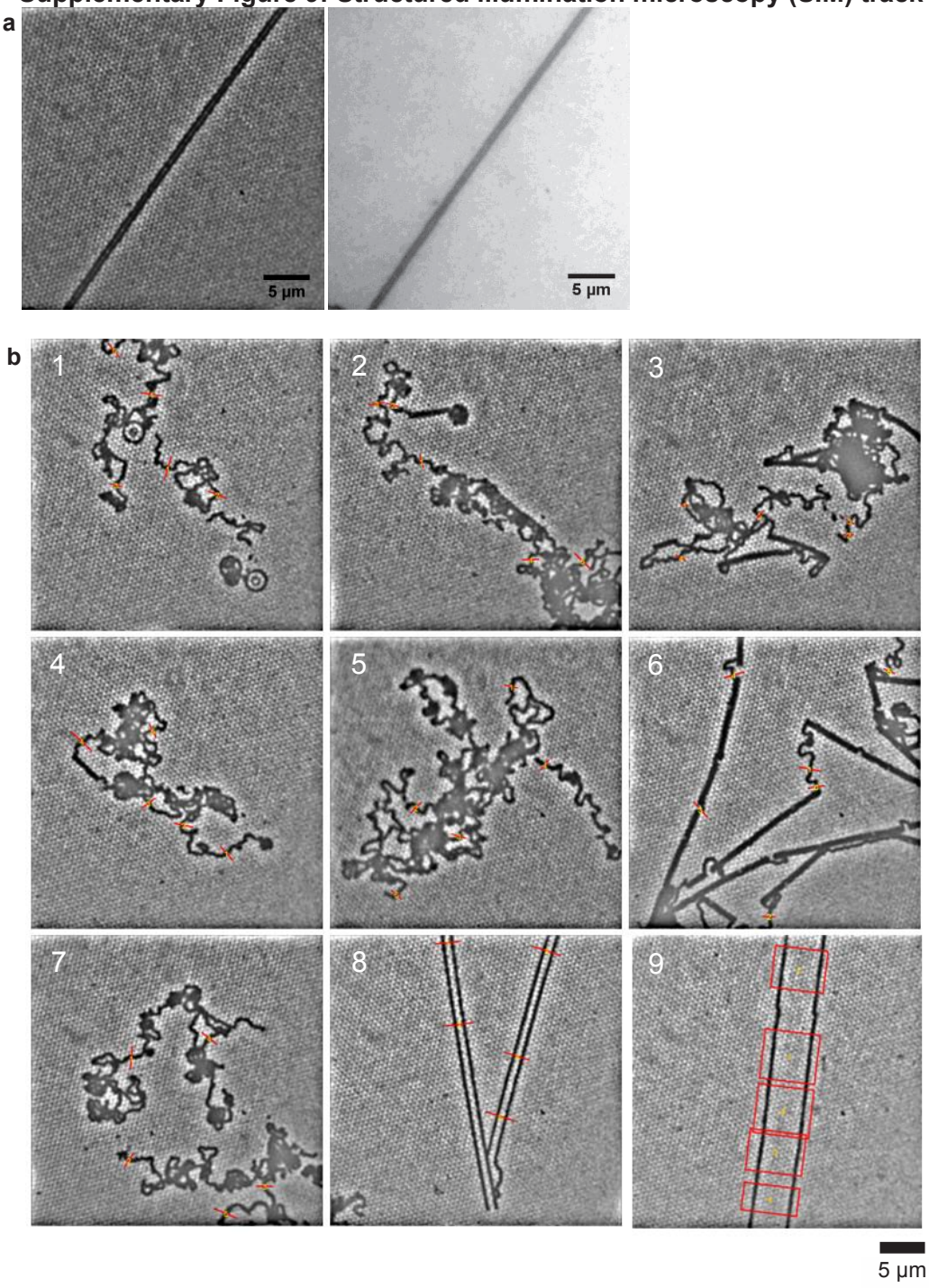


**Supplementary Figure 9. a**, Comparison between widefield (left) and super resolution SIM (right) microscopy images of a representative linear fluorescence depletion track. Data was obtained after incubating the RNA substrate with DNA-modified particles and RNase H for ~2 hr. **b**, Collage of SIM microscopy images of fluorescence depletion tracks used for histogram analysis of average FWHM of path width. In these representative examples, images 1-9, there are a variety of diffusive behaviors. Image 1-5 represent mostly self-avoiding tracks, while image 6 is primarily comprised of ballistic (linear) tracks with some periods of self-avoiding diffusion. Image 7 shows

a self-avoiding track. Finally, images 8 and 9 show ballistic or linear tracks generated by dimerised particles. The range of behavior observed here are consistent with the distribution of diffusional exponents obtained from Brightfield single particle tracking analysis (**Supplementary Fig. 11**). Note that the hexagonal patterns are a typical artefact of SIM due to the high-resolution reconstruction of the image.

DOI: 10.1038/NNANO.2015.259

**Supplementary Figure 10: Geometric model of particle hybridization with the surface**
A geometric model was constructed to validate the DNA compression/stretching required to produce a path width of ~380 ± 50 nm as determined by super resolution SIM. **a**, When duplexes form between the particle and the planar substrate within a junction that has a specific path width, then the difference in the height of the particle across this junction (L) must be equivalent to the maximum compression/stretching of the duplex. Based on the measured path width of 380 nm, L is expected to be 7.2 nm for the 5 μm particles (R= 2.5 μm) (see Equation 1). **b**, Plot showing the expected relationship between pathwidth and duplex stretching/compression.
Equation 1: $L = R - R * cos(sin^{-1}((0.5) * Path\ Width/R)))$

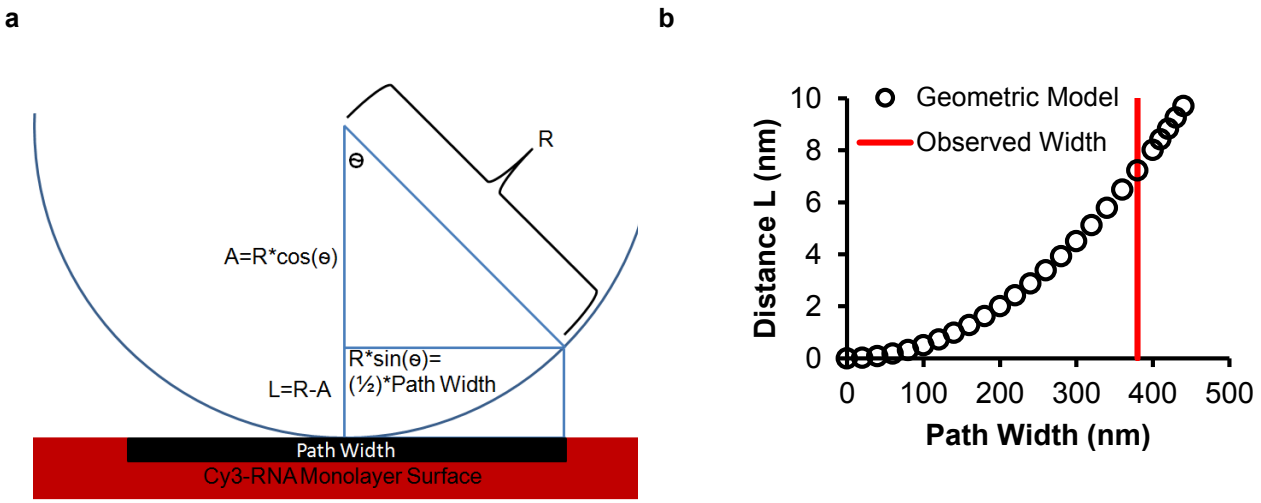


**Supplementary Figure 10. a**, Schematic of the geometric model used to determine the compression/stretching of the DNA/RNA duplex and single stranded segments as a function of pathwidth. **b**, Plot showing representative distances L as a function of pathwidth for a 5 μm particle. Highlighted in red is the experimentally observed pathwidth determined by SIM microscopy. Note that the expected pathwidth for particles of different diameters can be estimated using this same approach.

**Supplementary Figure 11: Histogram analysis of diffusional exponents**

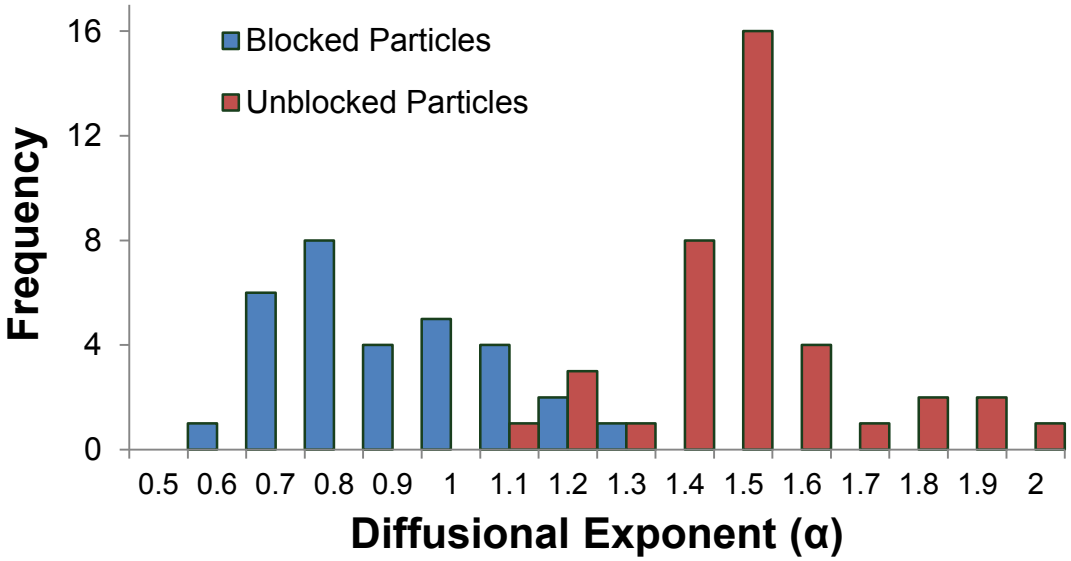


**Supplementary Figure 11.** Histogram analysis showing the distribution of diffusional exponents for blocked (blue) and unblocked (red) particles. The distribution reflects the degree of self-avoidance.

DOI: 10.1038/NNANO.2015.259

**Supplementary Figure 12: Displacement distributions from particle tracking and analytical expressions**

Particle displacements along a particular direction are indicative of particle behavior. For particles obeying pure diffusion, the probability distribution of displacements shows Gaussian scaling for a fixed time interval.

$$P(x,t) = \frac{1}{\sigma\sqrt{\pi}} e^{-x^2/\sigma^2} = \frac{1}{\sqrt{4\pi Dt}} e^{-x^2/4Dt}$$

where $x$ is the displacement in either the horizontal ($\Delta x$) or vertical ($\Delta y$) direction, $t$ is the time interval, $\sigma^2=4Dt$ is the variance, $D$ is the diffusion constant, and $P$ is the probability density function (PDF).

Panel **a** shows the experimental probability distribution of particle displacements for RNase H powered monowheels for a 50 s (10 frame) time interval. The large-displacement tails capture motion over longer distances. The tails fit well to

$$P(x) = P(0)e^{-A|x|^{\nu}}$$

with $\nu = 4.3 \pm 1$. This value is significantly different than the Gaussian value of $\nu = 2$, which indicates that the particles do not execute simple diffusive motion. In addition, this is similar to what is expected for self-avoiding chains.[5] Note that self-avoiding chains and walks are different (see **Supplementary Discussion 1**).

Panel **b** shows the corresponding distribution for particles whose unbound DNA was blocked by hybridization with a complementary DNA strand. A fit to the tails yields $\nu = 1.8 \pm 0.8$, which confirms that particles in this experiment execute simple diffusive motion.

Both distributions show two behaviors, one at small displacements and the other at large displacements. The two behaviors are indicative of two processes happening, or two states of motion. This is consistent with the fact that the velocity distributions also have two modes (**Fig. 3d, e**). These features of the displacement and velocity distributions also persist at the single particle level (**Supplementary Fig. 16**). Further investigation would be needed to understand the origin of these features.

To ensure that $\nu = 4$ is not an artefact of a particular time interval, we analysed the time dependence of $\sigma$ across all time intervals. If $\nu = 4$ and MSD is proportional to $t^{1.5}$ (**Supplementary Discussion 1**), then $\sigma$ should be proportional to $t^{0.75}$ (based on the derivation below). We find that experiments agree well with this scaling in $\sigma$ (**Supplemental Fig. 12c**).

Consider the general case where x has the exponent v. Here, the probability density function is:

$$P_{\nu}(x,t) = \frac{\nu}{2\sigma\Gamma(1/\nu)} e^{-|x|^{\nu}/\sigma^{\nu}}$$

where σ has a time dependence, σ(t), and $\Gamma$ is a gamma function.[5] If $\nu$ is equal to 4 for self-avoiding motion (**Supplemental Fig. 12a** and **Supplementary Discussion 1**), upon integrating we get:

$$< x^2 >= \int x^2 P(x,t)dx \propto \sigma^2$$

We also know from our experiments and simulations (**Supplementary Discussion 1**) that $x^2(t) \propto t^{1.5}$. By substituting $\sigma^2$ for $x^2$, we get $\sigma \propto t^{0.75}$.

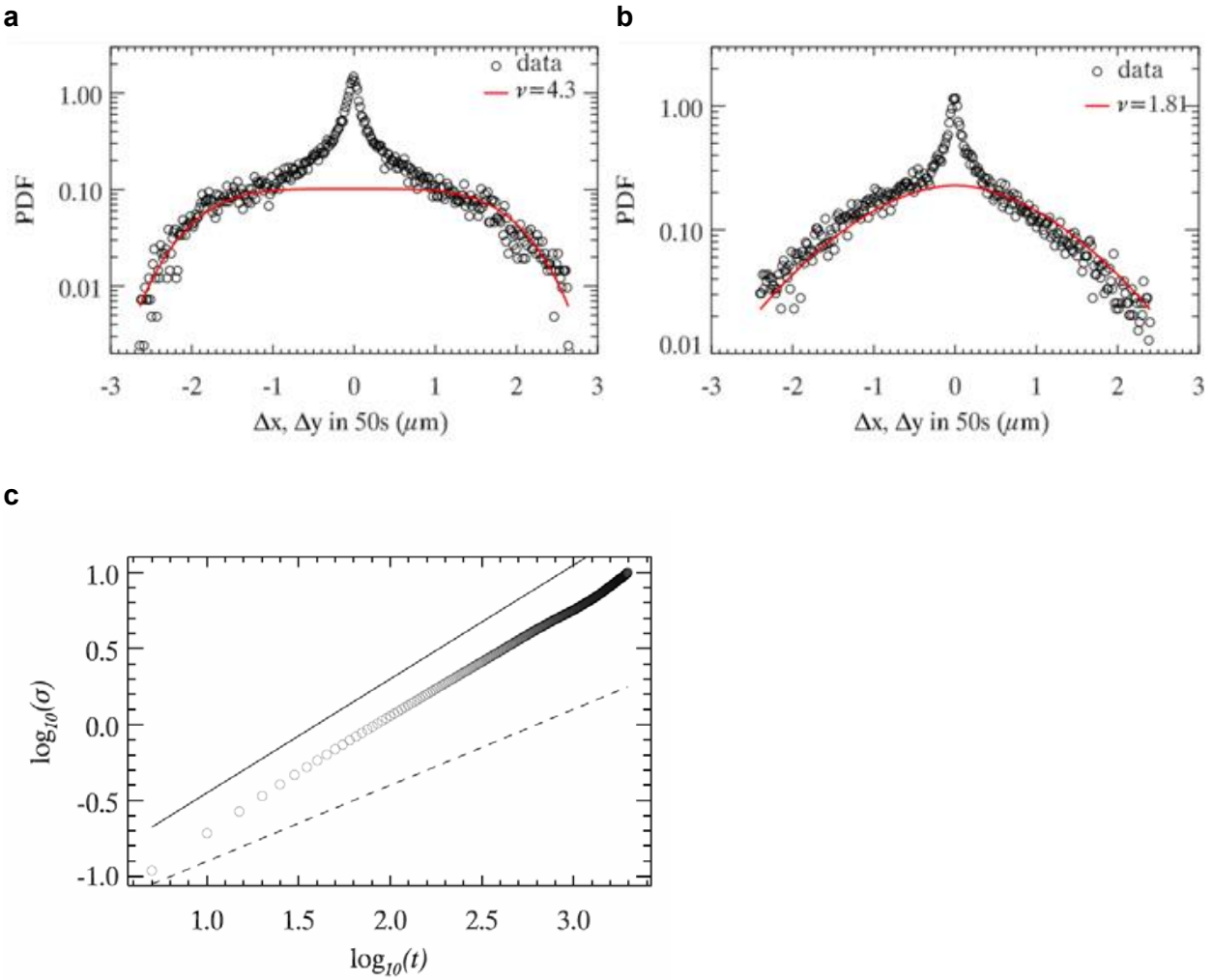


**Supplementary Figure 12.** Probability distribution of displacements from **a** DNA modified particles and **b** particles whose unbound DNA was blocked by hybridization with a complementary DNA blocking strand. **c** A plot showing the log($\sigma$) vs log($t$) dependence. The straight line is the expected slope for self-avoiding diffusion (0.75), the dashed line is the slope for random diffusion (0.5), and the circles are the data for unblocked particles. The slope for experimental data (circles) fits well with the slope for self-avoiding diffusion, thus validating our expectations.

DOI: 10.1038/NNANO.2015.259

**Supplementary Figure 13: Schematic showing potential mechanisms of particle translocation**

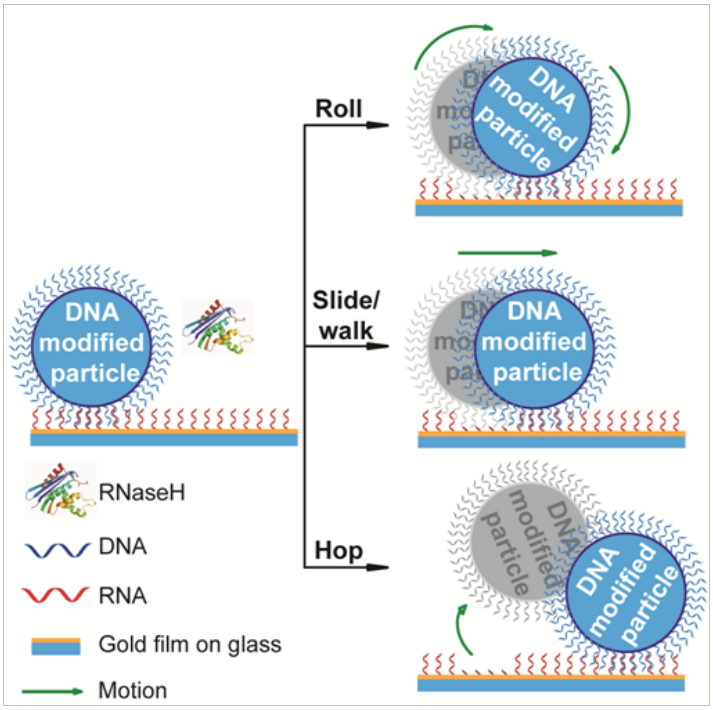


**Supplementary Figure 13.** A schematic illustrating the potential mechanisms of particle motion (green arrow). If $k_{cat}$ and $k_{off}$ are faster than $k_{on}$, then particles should hop (scenario shown at bottom) and if $k_{cat}$ and $k_{off}$ are slower than $k_{on}$, then particles should roll or slide/walk (top two scenarios).

**Supplementary Figure 14: Proposed mechanism of translocation**

Experimentally, we observed that particle velocity slowed by 50% to 1 ±1 μm/min when [KCl] was increased from 37 mM to 150 mM (**Fig. 3d**). This suggests that the slow step in translocation is $k_{off}$, rather than $k_{on}$, assuming that RNase H activity remains constant. In addition, we found that particle velocity is highly sensitive to divalent ion concentration (**Supplementary Fig. 15**). Finally, to investigate the effect of $k_{cat}$ on motor velocity while minimally perturbing other kinetic parameters, we tuned the pH since this is known to strongly modulate enzyme activity.[6] When the pH was decreased from 8.0 to 7.5, the $k_{cat}$ decreased by ~6 fold from 25 $min^{-1}$ to 4 $min^{-1}$, while the particle velocity remained the same (**Fig. 3e**). In contrast, further decreasing the pH to 7.0, where the $k_{cat}$ drops by another ~10 fold led to a 3 fold decrease in particle velocity from 2 ± 0.4 μm/min to 0.7 ± 0.1 μm/min. Taken together, these results indicate that $k_{off}$ acts as the kinetic bottleneck for particle motion at elevated pH, while lower pH (pH < 7.0) places $k_{cat}$ as the rate limiting step in translocation

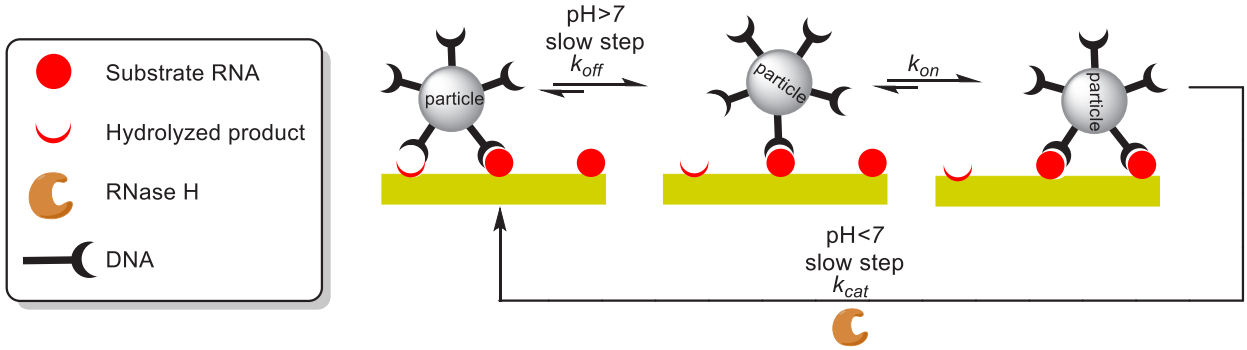


**Supplementary Figure 14.** Schematic of the proposed mechanism for particle translocation. For simplicity, the multivalent interaction with the surface has been reduced down to a divalent interaction.

DOI: 10.1038/NNANO.2015.259

**Supplementary Figure 15: Motor velocity magnesium dependence**

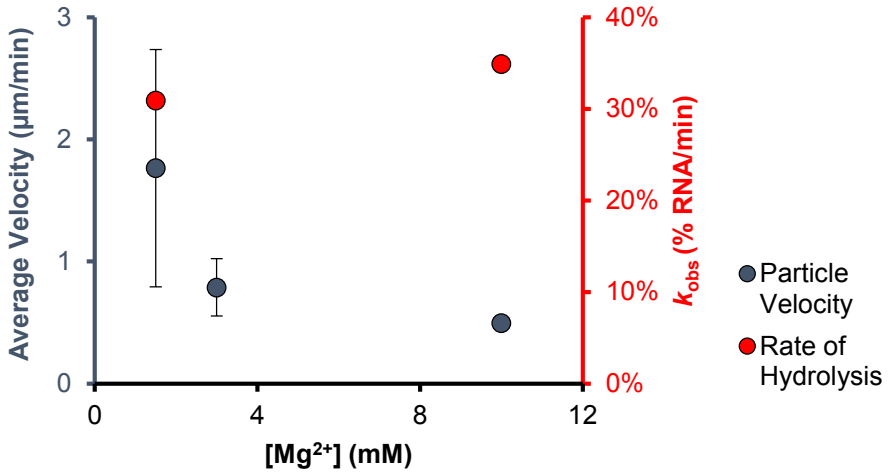


**Supplementary Figure 15.** A plot summarizing the average particle velocity and observed rate of RNA hydrolysis as a function of [$Mg^{2+}$] concentration. The error bars represent the standard deviation for the particle velocities for all the particles (typically $n$ >15) at each 5 s interval for the 30 min time-lapse video. When [$Mg^{2+}$] was slightly increased from 1.5 mM to 3 mM, a dramatic 2.3 fold reduction in particle velocity was observed (down to 0.8 ±0.2 µm/min); whereas, the observed rate of RNA hydrolysis increased slightly. This suggests that divalent charge screening tends to increase non-specific particle-substrate interactions.

## Supplementary Figure 16: Individual particle velocity histogram analysis

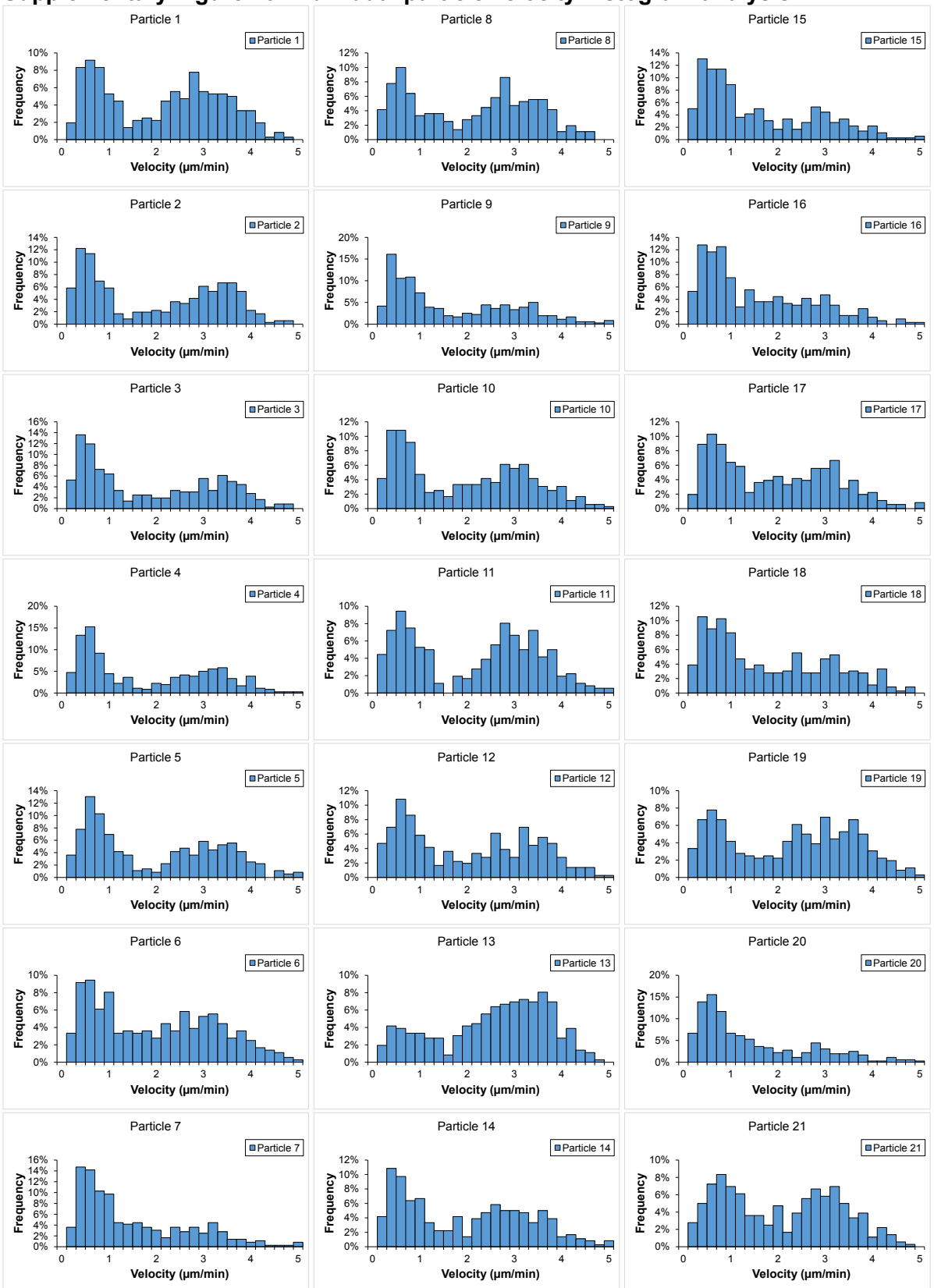

DOI: 10.1038/NNANO.2015.259

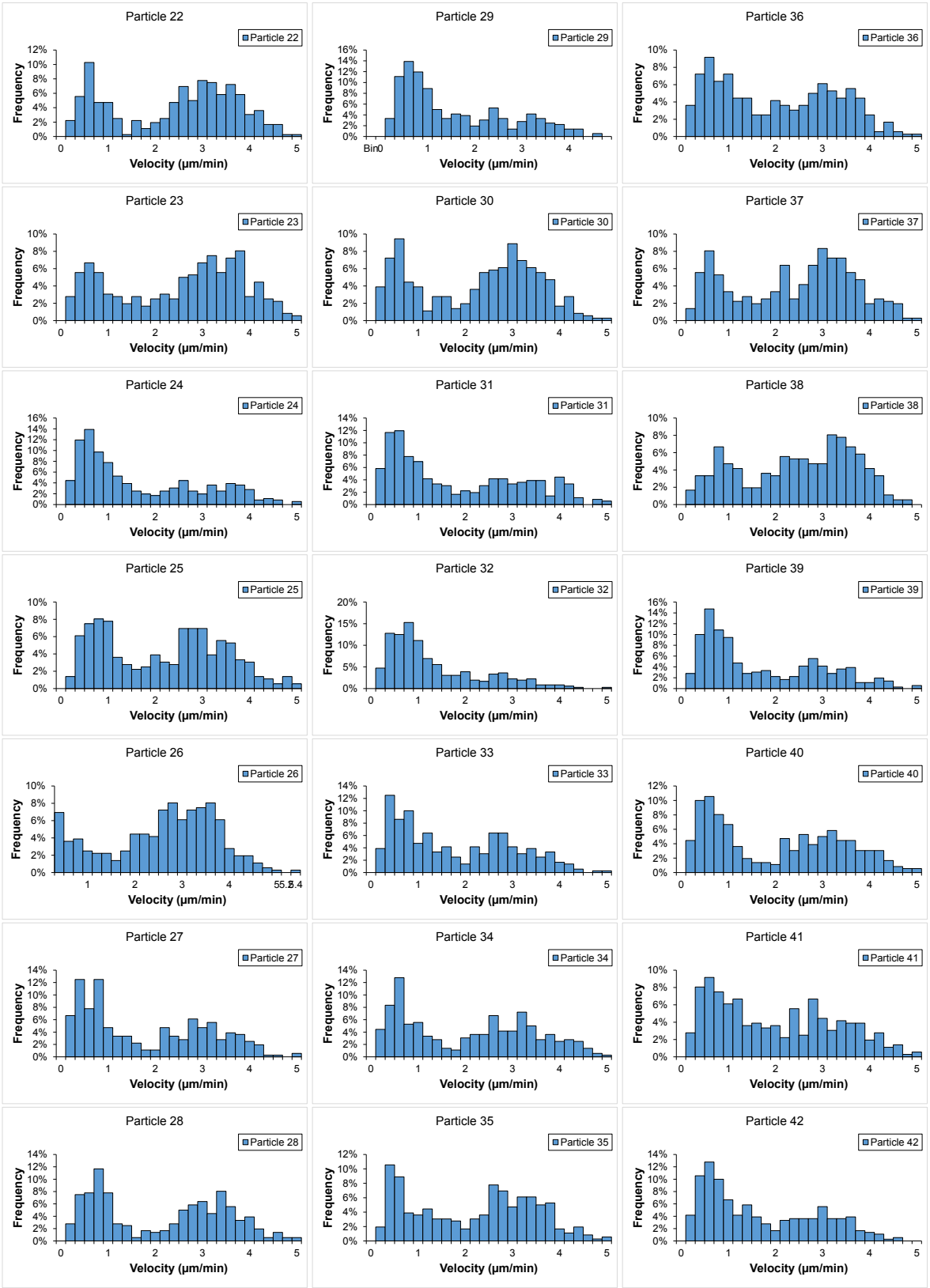


**Supplementary Figure 16.** Histogram analysis of individual particle velocities (25 mM Tris pH 8.0, 8 mM NaCl, 37.5 mM KCl, 1.5 mM $MgCl_2$, 10 vol % formamide, and 0.75% (g/mL) Triton X).

**Supplementary Figure 17: Effect of RNase H concentration on monowheel velocity**

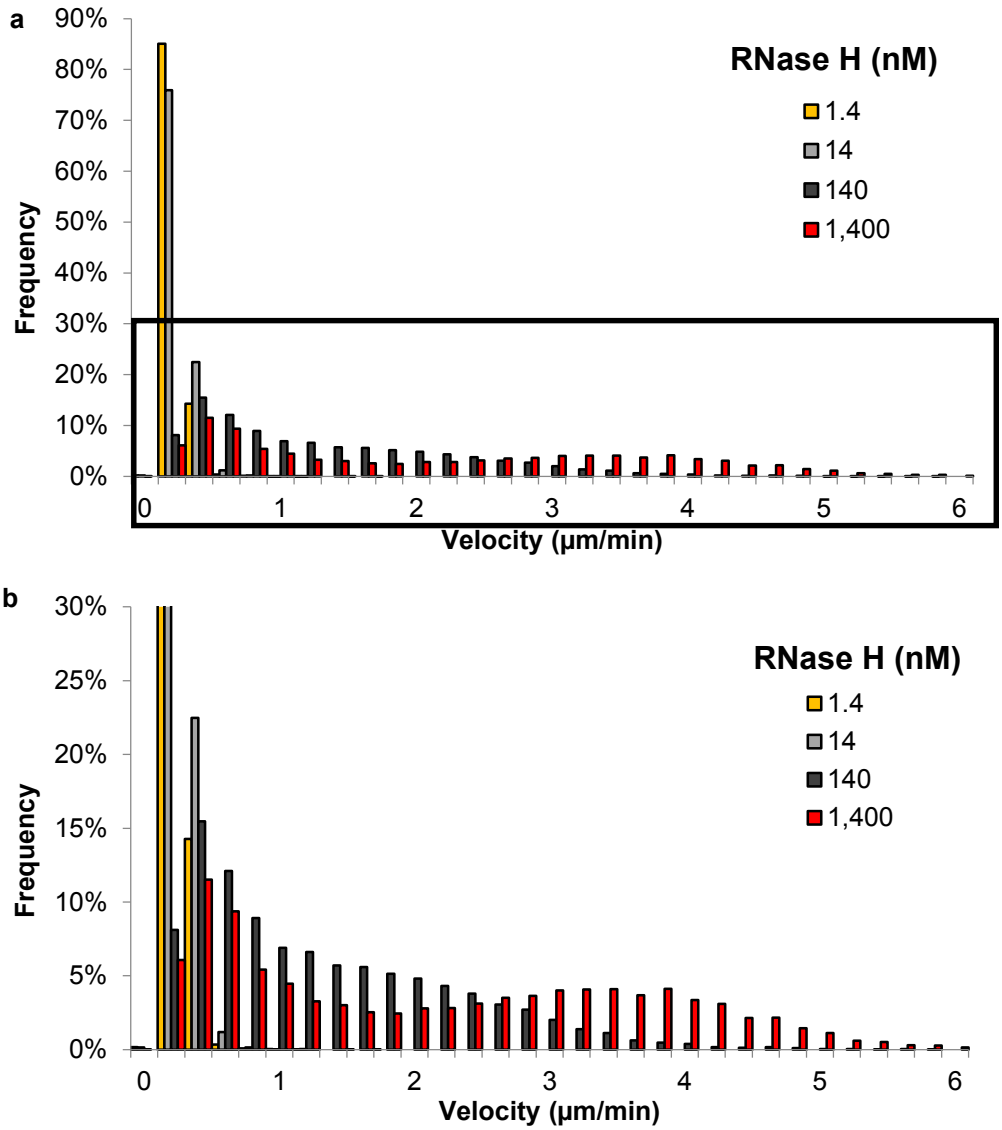


**Supplementary Figure 17. a,** Histogram analysis of particle velocity for each 5 s interval of particles with varying RNase H concentrations. **b,** Expanded view of the inset region.

DOI: 10.1038/NNANO.2015.259

**Supplementary Figure 18: Effect of gravity on monowheel velocity**

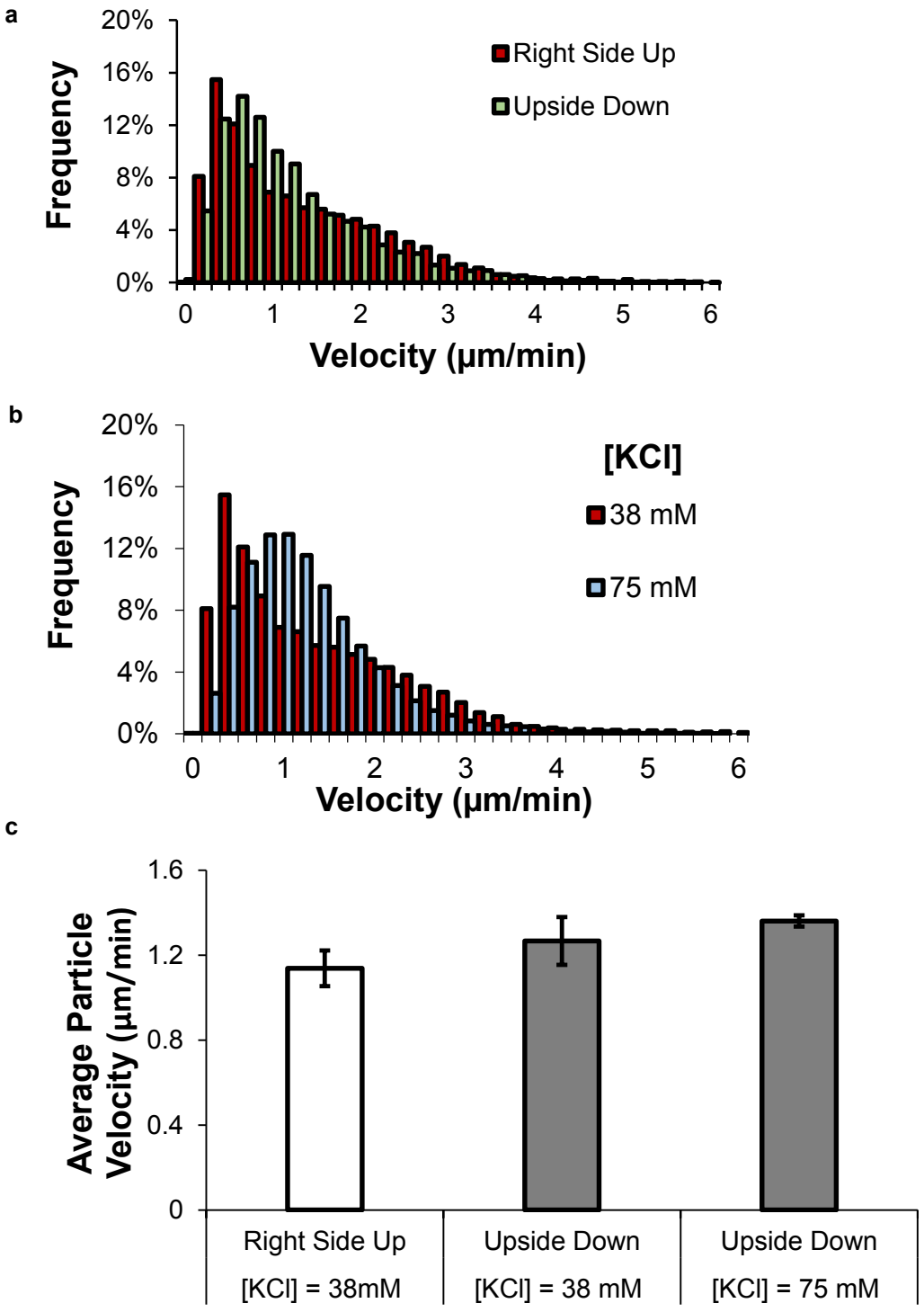


**Supplementary Figure 18. a,** Histogram analysis of particle velocity for each 5 s interval of particles rolling against the force of gravity (green, *n* = 16 (5,760 occurrences)) or with the force of gravity (red, *n* = 20 (7,200 occurrences)) at [KCl] = 38 mM. **b,** Histogram analysis of particle velocity for each 5 s interval of particles rolling against gravity as a function of [KCl]; 38 mM (red, *n* = 16 (5,760 occurrences)) and 75 mM (blue, *n* = 50 (18,000 occurrences)).

**Supplementary Figure 19: Effect of particle size on velocity**

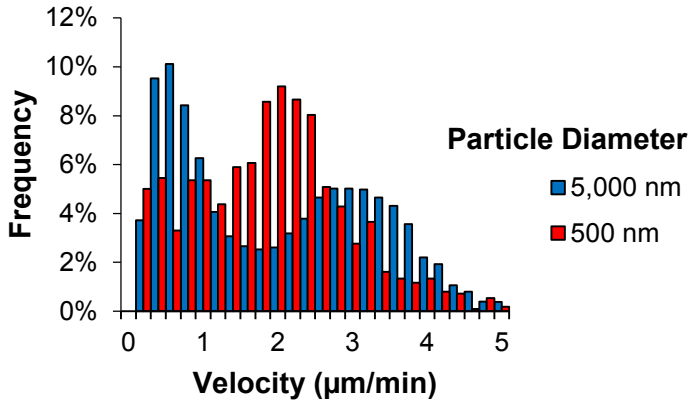


**Supplementary Figure 19.** Histogram analysis of particle velocity for each 5 s interval as a function of particle size (5,000 nm diameter; blue and 500 nm diameter; red).

DOI: 10.1038/NNANO.2015.259

**Supplementary Figure 20: Monowheel average run lengths**

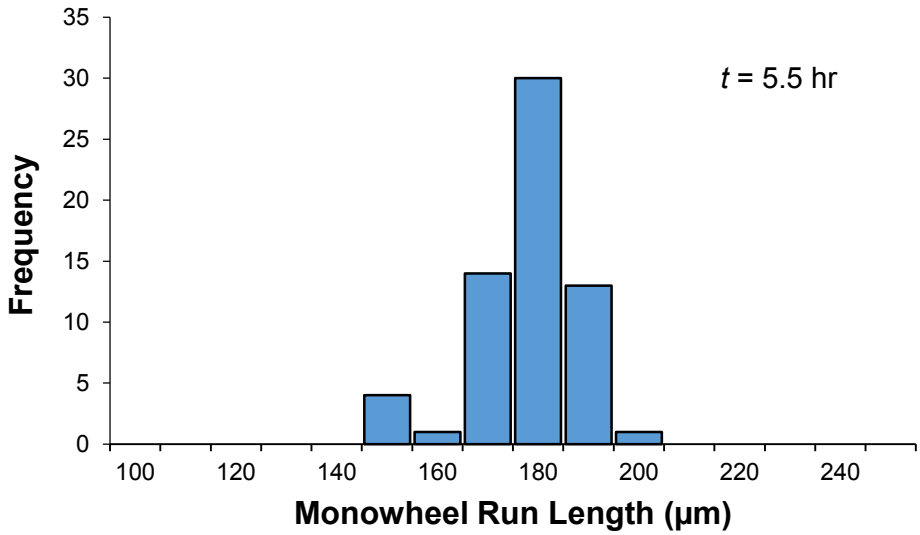


**Supplementary Figure 20.** Histogram analysis of average monowheel run length after 5.5 hrs. Only 10% of monowheels remained in motion after 12 hrs, which may be due to enzyme denaturation.

**Supplementary Figure 21: Effect of particle shape on mobility**

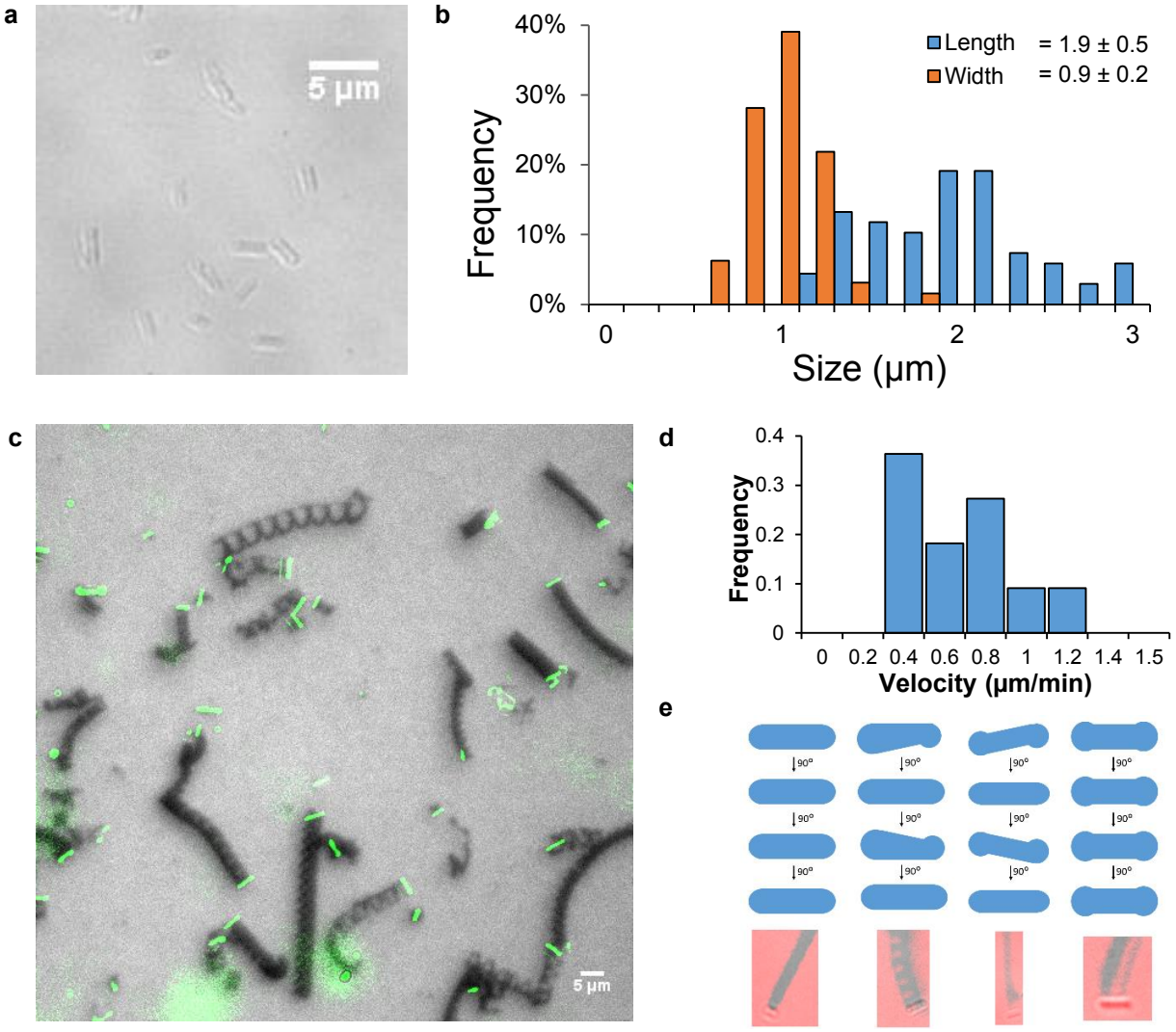


**Supplementary Figure 21. a**, Representative brightfield image of DNA functionalised sililca micro-rods. Rods were synthesised via emulsion based method[7] and were surface functionalised with APTES.[8] The resulting aminated rods were functionalised with DNA using the same methods described previously (NHS-azide amine coupling followed by azide-akyne Huisgen cycloaddition). **b**, Corresponding histogram analysis characterizing the DNA functionalised micro-rods' length and width. **c**, Representative overlay of a brightfield (green) and fluorescence (gray) image showing microrod trajectories (fluorescence depletion) at $t$ = 45 min. **d,** Histogram analysis of average particle velocity. **e**, Proposed model showing how particle imperfections can lead to spiral like structures.

DOI: 10.1038/NNANO.2015.259

**Supplementary Figure 22: SNP sensing using a microscope and a smartphone readout**

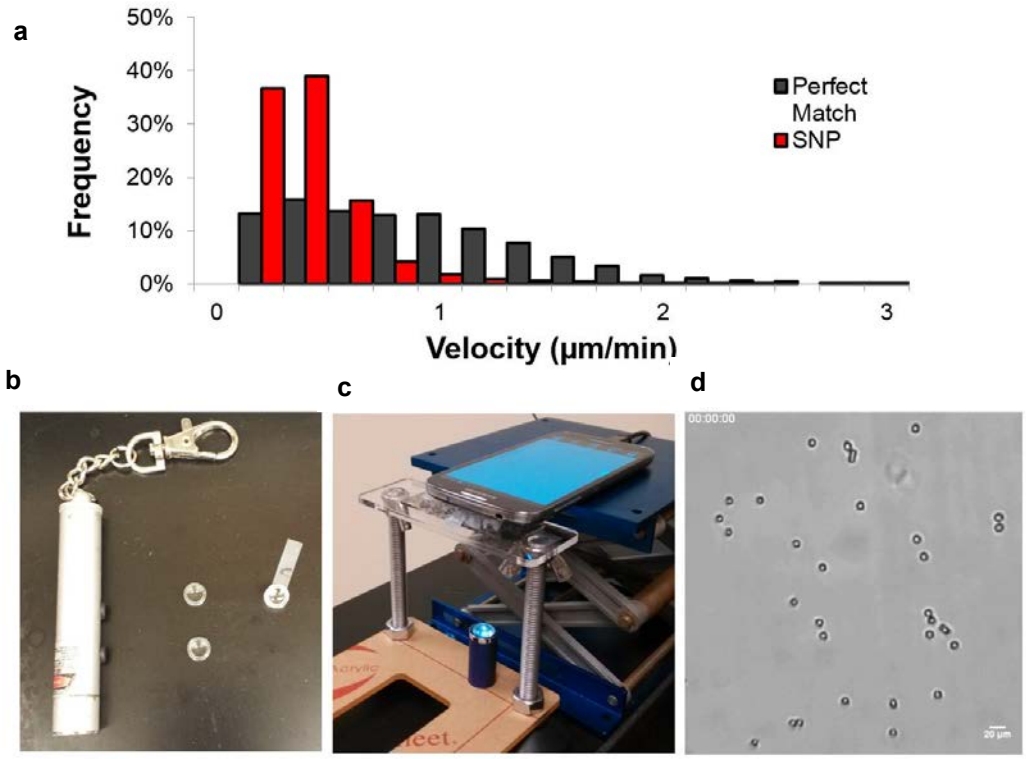


**Supplementary Figure 22. a**, Histogram analysis of particle velocities obtained for each 5 s interval for particles functionalised with DNA fully complementary to the RNA substrate (Perfect Match, red, *n* = 36 particles) and DNA that contains a single base mismatch (SNP, red, *n* = 23 particles). Velocities were obtained by tracking the particle through BF using the smartphone microscope. Note that due to the shorter recognition sequence, higher salt concentrations were used in the reaction buffer (75 mM Tris (pH = 8), 110 mM KCl and 4.5 mM $MgCl_2$). **b**, A photograph of the plastic magnifying lenses obtained from a toy laser pointer ($2). These lenses were used to image the particles with a smartphone camera (**Figure 5**). **c**, A photograph of the smartphone microscope set up used to illuminate and focus onto the sample. **d**, Representative smartphone image of the 5 μm particles in the SNP assay.

**Supplementary Figure 23: SNP detection without non-natural modifications to the DNA**

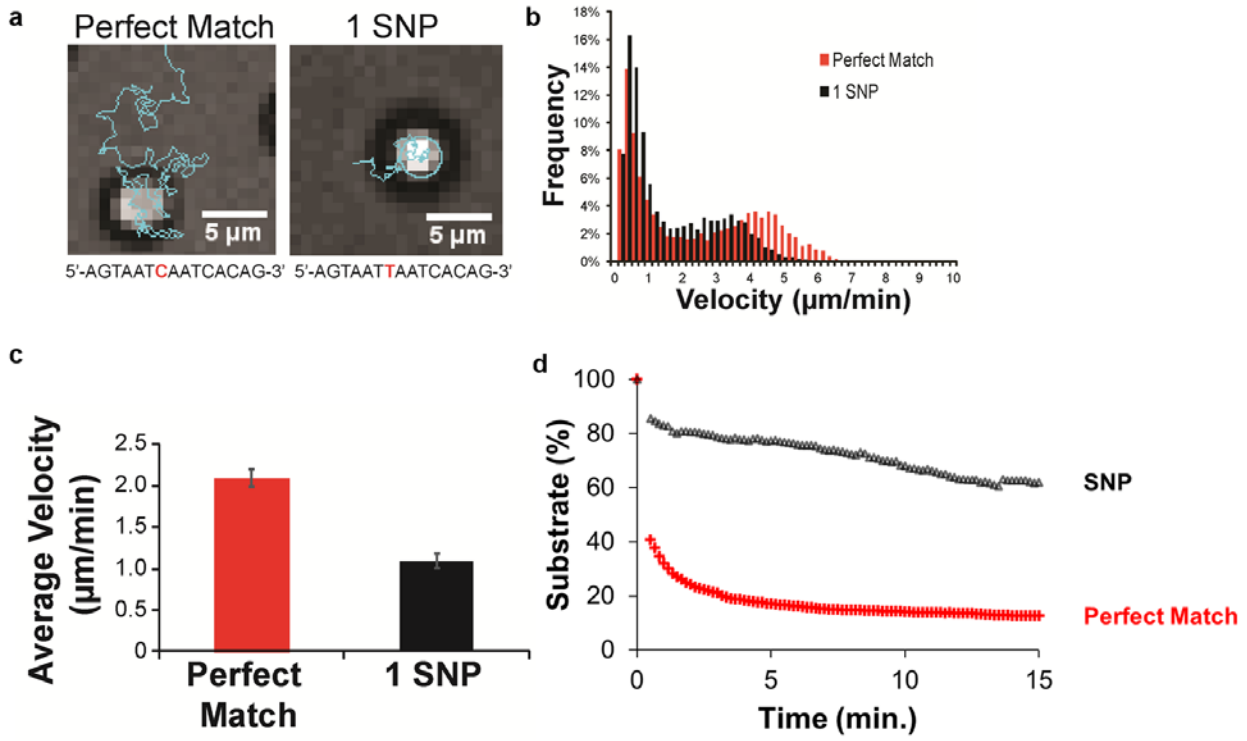


**Supplementary Figure 23. a**, Representative brightfield trajectories of RNase H driven particle motion for particles modified with fully complementary DNA (perfect match) to the RNA monolayer or DNA with a SNP mutation (1 SNP). **b**, Histogram analysis of particle velocities for perfect match (red, *n* = 10 particles (3,600 occurrences)) and 1 SNP (black, *n* = 13 particles (4,680 occurrences)) modified particles. **c**, A bar graph showing the average velocities for perfect match (red) and 1 SNP (black) modified particles. **d**, A kinetic plot showing the rate of RNA hydrolysis for a monolayer of RNA-DNA duplexes that are fully complementary (red) or containing a SNP mutation (black) upon addition of RNase H.

DOI: 10.1038/NNANO.2015.259

## Supplementary Discussion 1: Theory and simulations of self-avoiding particle rollers

*True self-avoiding walk*

To investigate whether our particles exhibit self-avoiding behavior, we first performed a simple simulation of a self-avoiding random walk. A particle starts at the origin of a two-dimensional square lattice. At each fixed time step, the particle moves with equal probability to any one of its neighboring sites that has not been occupied in the past. The particle eventually traps itself, which marks the end of the simulation (**SD Fig. 1a**).

Self-avoiding walks have been well studied in polymer physics, since a polymer is a chain that cannot overlap with itself. However, there is an important difference between a self-avoiding chain and a self-avoiding walk. The first is a physical object; the second is a dynamic process. In general, when self-avoiding walks are discussed in the literature, this typically refers to self-avoiding (polymer) chains. The dynamic process is usually distinguished from self-avoiding polymer chains by being described as the "true" or "myopic" self-avoiding walk. Here, we are studying the dynamic process, the "true" self-avoiding walk.

The difference arises at the level of statistics. Averaging over all possible configurations of a length $t$ chain, the mean squared displacement (MSD) from end-to-end scales in two dimensions as MSD ~ $t^{3/2}$. However, this is not true for the walk. The reason is that when dynamically generating the walk by taking random steps, one does not sample all $t$-step configurations equally[9]. The result is that the MSD for the walk in two dimensions scales with time $t$ as MSD ~ $t$ log($t$) for large values of $t$ [10, 11].

**SD Fig. 1b** shows MSD versus time for the simulation, averaging over 1000 particles, using time differences at any point along the path. Note that at sufficiently long times, the simulation follows the expectation MSD ~ $t$ log($t$). For comparison, we also show the expectations for ballistic motion (MSD ~ $t^2$) and diffusive motion (MSD ~ $t^1$).

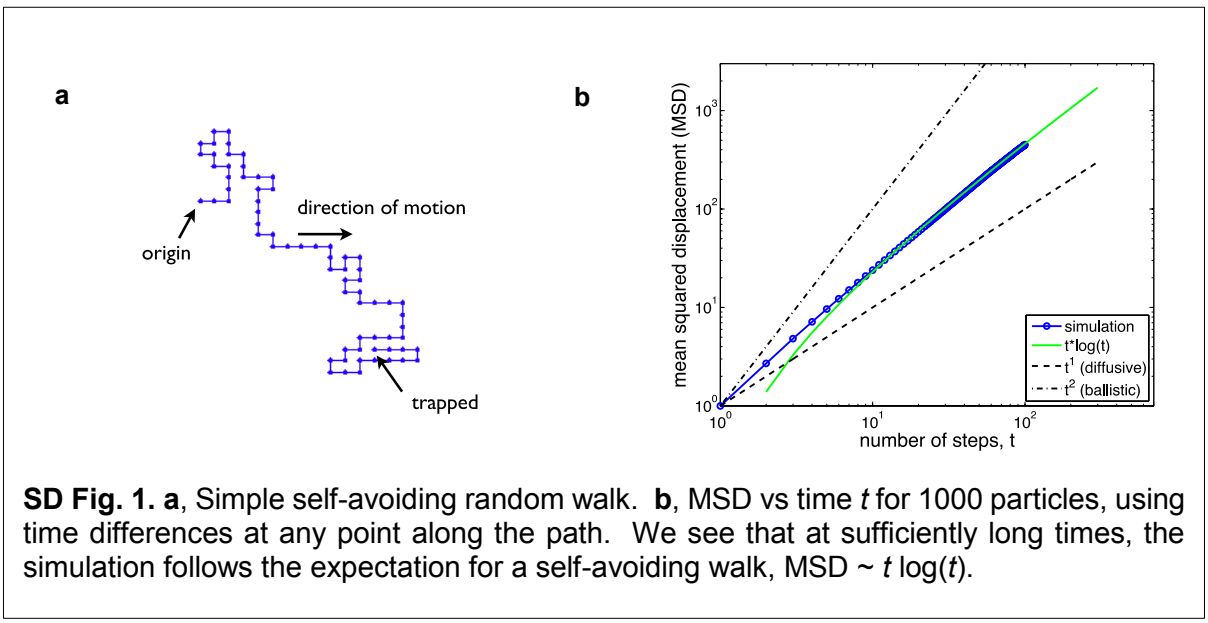


**SD Fig. 1. a**, Simple self-avoiding random walk. **b**, MSD vs time $t$ for 1000 particles, using time differences at any point along the path. We see that at sufficiently long times, the simulation follows the expectation for a self-avoiding walk, MSD ~ $t$ log($t$).

*Multivalency and enzyme kinetics*

The simple simulation in the previous section lacks two key features of the experimental particles. First, the particles are multivalent, meaning they bind the surface at many points at any given point in time. Second, their motion is driven by enzymatic hydrolysis, such that the timing of unbinding events is not fixed but rather depends on stochastic chemical kinetics. Here we incorporate both features into the simulation.

Multivalency is incorporated by allowing the particle to bind at more than one site at a time (**SD Fig. 2a**). Sites are distributed on a square lattice. No two concurrently bound sites may be separated by a distance larger than the path width, which is measured experimentally.

Stochastic kinetics are incorporated by drawing unbinding times from a probability distribution. As suggested experimentally, we assume that a single slow step sets the unbinding rate $k$. Unbinding times are then drawn from an exponential distribution with mean $1/k$. Once a sufficient number of unbinding events occur, the particle may access new sites within the path width constraint. These sites are bound in a random order until the constraint is satisfied. Binding is modelled as instantaneous because the binding time (on the order of microseconds) is significantly shorter than the unbinding time (on the order of seconds). The ensuing particle dynamics are illustrated in **Supplementary Movie 11**.

**SD Fig. 2b** shows MSD versus time for the simulation with multivalency and stochastic kinetics, averaging over 733 particles, using time differences at any point along the path. We see that the simulation exhibits two regimes. At short times, the particles exhibit diffusive behavior (MSD ~ $t^1$). This is due to the small random movements that accompany individual unbinding events. Individual events do not appreciably change the particle's mean position at short times, but instead introduce short-range diffusive "noise" (**Supplementary Movie 11**). At long times, the particles exhibit self-avoiding behavior (MSD ~ $t \log(t)$). This is because on length scales larger than the path width (380 nm), the particle effectively executes a self-avoiding random walk. **SD Fig. 2b** thus demonstrates that on sufficiently long length and time scales, self-avoiding behavior persists even with multivalency and stochastic kinetics.

DOI: 10.1038/NNANO.2015.259

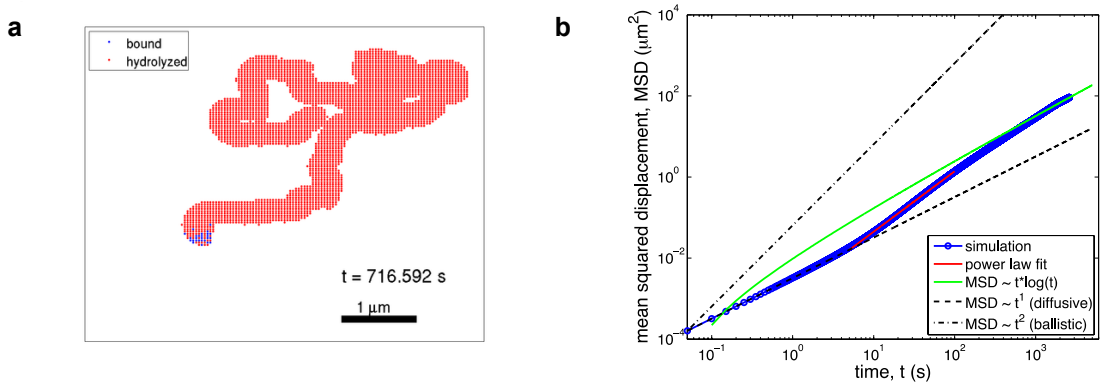


**SD Fig. 2. a**, Snapshot of a multivalent stochastic self-avoiding walk. **b**, MSD vs time $t$ for 733 particles, using time differences at any point along the path. We see two regimes: diffusive behavior at short times (MSD ~ $t^1$) and self-avoiding behavior at long times (MSD ~ $t\log(t)$). Data from 5 s to 100 s fits well to a power law MSD ~ $t^\alpha$ with $\alpha$ = 1.49 ± 0.05, where the mean and standard deviation are computed across 569 individual particle runs that each last longer than 500 s.

Particle tracking experiments allow for measurement of the MSD over time windows from 5 s to 100 s, revealing a power law scaling MSD ~ $t^\alpha$ with $\alpha$ = 1.45 ± 0.2 (main text **Fig. 2f**). In this range of time windows, the simulation data also fit well to a power law, with $\alpha$ = 1.49 ± 0.05 (**SD Fig. 2b**). The agreement demonstrates that experimental particle motion is statistically consistent with a multivalent self-avoiding walk.

The results in **SD Fig. 2** are obtained with a multivalency of $s$ = 10 lattice sites per path width, which is the highest computationally tractable value. However, in experiments, the measured path width of 380 nm and the substrate footprint of 20 nm$^2$ imply that the multivalency could be as high as s = (380 nm)/√(20 nm$^2$) = 85. Therefore, we tested the dependence of the MSD statistics on the multivalency for the tractable values $s$ = 4 to 10. **SD Fig. 3** shows that the fitted power $\alpha$ is largely independent of multivalency, suggesting that our simulation provides a good model for the experiment, even if the experimental multivalency is higher than $s$ = 10. The reason that the statistics are independent of multivalency is that at long length and time scales, the particle essentially moves via a rolling mechanism. This means that if the particle is rolling in a particular direction, time between when a contact binds at the front and when it unbinds at the back is independent of the number of other bound sites (see *Velocity estimate* below for further discussion).

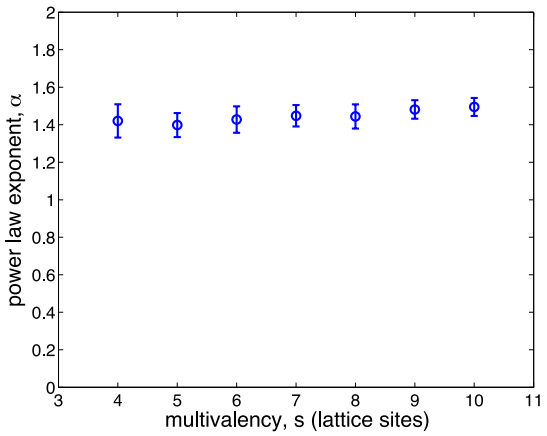


**SD Fig. 3:** MSD power-law exponents $\alpha$ as a function of multivalency $s$, defined as the number of lattice sites per path width. Path width is kept constant at $w$ = 380 nm while $s$ is varied. For each value of $s$, exponents and standard deviation are computed from between 20 and 85 particle runs that last longer than 500 s, using time windows between 5 s and 100 s. We see that the exponent is largely independent of the multivalency.

*Displacement distribution*

Our multivalent stochastic simulation also permits a comparison with the experimentally measured distribution of particle displacements (**Supplementary Fig. 12**). There we found that large displacements $x$ are well described by the form $P(x) = P(0)\exp(-A|x|^{v})$ with $v = 4.3 \pm 1$. **SD Fig. 4a** shows the distribution of displacements in 50 s from simulations of 733 particles, using time differences at any point along the path. To determine whether the above functional form provides a reasonable fit, we note that it can be rewritten as $\log[P(0)/P(x)] = A|x|^{v}$, which means that a plot of $\log[P(0)/P(x)]$ versus $|x|$ should be linear on a log-log scale, with slope $v$. **SD Fig. 4b** shows this plot, demonstrating that the dependence is indeed linear for sufficiently large $|x|$ (i.e. in the tails of the distribution). The slope is $v = 3.8 \pm 0.1$, which agrees with the experimental value of $v = 4.3 \pm 1$. The agreement further supports the statistical consistency of our particle motion with self-avoiding behavior.

DOI: 10.1038/NNANO.2015.259

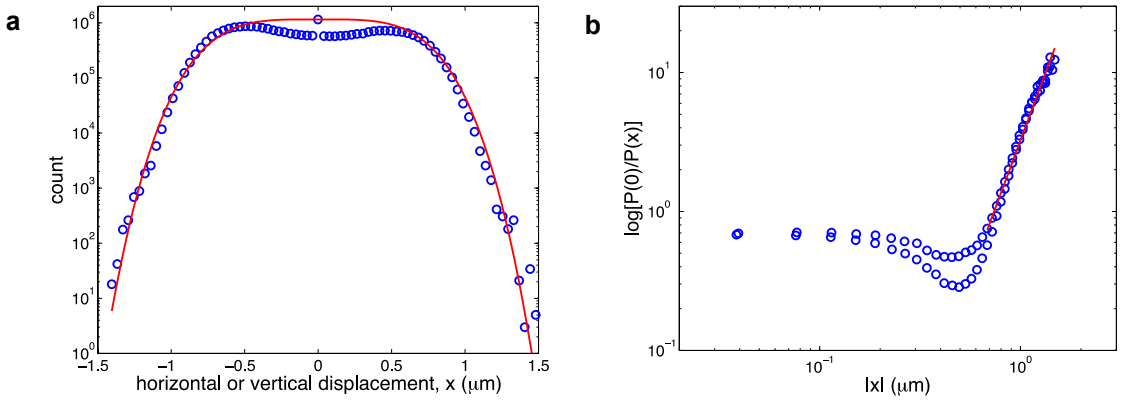


**SD Fig. 4. a**, Distribution of particle displacements $x$ in 50 s. 733 particles are used, using time differences at any point along the path. Red curve shows fit to $P(x) = P(0)\exp(-A|x|^{v})$ with $v = 3.8 \pm 0.1$. **b**, The parameter $v$ is obtained by fitting the linear region of the plot of $\log[P(0)/P(x)]$ versus $|x|$ on a log-log scale.

*Velocity estimate*

Here we present a rough estimate of the particle velocity based on the enzyme kinetics. Unbinding occurs at a rate on the order of $k \sim 10$/min. As mentioned above, the multivalency could be as high as $s = 90$ binding sites per path width. Thus, a naïve argument might suggest that moving one path width $w = 380$ nm requires $s = 85$ unbinding times, or $s/k = 8.5$ min, corresponding to a velocity of roughly 45 nm/min. This is much slower than the experimentally measured velocity of 2 μm/min.

However, the above argument neglects the processivity of the rolling process. To understand this point, we consider the limit of a fixed unbinding time and ballistic motion. In this limit, contacts bind and unbind sequentially in the direction of motion. This means that by the time a particular contact unbinds, all contacts behind it have already unbound, and all contacts in front of it have yet to unbind. In particular, this means that the time between when a contact binds in front, and when the same contact unbinds in back, is equal to one unbinding time $1/k$. In this time, the particle has moved one path width $w$, and thus the velocity is $wk = 3.8$ μm/min. Because in reality unbinding is stochastic, and motion is not completely ballistic, this estimate is an upper bound. Nonetheless, it much more closely reflects the measured value of 2 μm/min.

The above argument implies that particle motion is largely independent of multivalency $s$, due to the processivity of the rolling process. That is, the particle rolls one path width per unbinding time, no matter how many contacts are bound within the path. Indeed, this provides an explanation for why the statistics of particle motion in the simulation, as captured by the MSD, are largely independent of multivalency (**SD Fig. 3**).

## Supplementary Discussion 2: Power conversion efficiency

The power conversion efficiency (η) for the monowheel motor can be quantified as described by Wang *et al.*[12]

$$\eta = \frac{\text{mechanical power output}}{\text{total chemical power input}} = \frac{P_{\text{mechanical}}}{P_{\text{chemical}}}$$

where $P_{\text{mechanical}}$ is defined as,

$$P_{\text{mechanical}} = F_{\text{drag}} v = \int v^2$$

$F_{\text{drag}}$ is the resistive force on the particle, $v$ is the particle velocity, and $\int$ is the friction coefficient. The particle velocity can directly be measured and the friction coefficient between a DNA modified silica bead and an RNA monolayer can be derived from the experimentally measured diffusion coefficient ($D$) using the Einstein diffusion relationship:

$$D = \frac{k_b T}{\int}$$

where $k_b$ is the Boltzmann constant and T is the temperature. The 2D diffusion coefficient was measured to be $D$ = 0.096 μm$^2$/s for DNA modified particles diffusing across an RNA monolayer, which was derived from the slope of the MSD versus time for randomly diffusing blocked particles (**Fig. 3**).

$P_{\text{chemical}} = n_{\text{RNA Hydrolysis}} \Delta_r{}^{\ominus}G$

Where $n_{\text{RNA Hydrolysis}}$ is the turnover number for hydrolysis and $\Delta_r{}^{\ominus}G$ is the Gibbs free energy for the hydrolysis of an RNA phosphodiester bond (30 kcal/mol).[13] The turnover number for RNA hydrolysis can be quantified from the particle velocity ($v$), contact diameter ($d$), and RNA density on the surface as detailed below:

$$n_{\text{RNA Hydrolysis}} = v * d * \frac{1\text{RNA}}{18\ \text{nm}^2} * \frac{\text{hydrolyzed phosphodiesters}}{\text{RNA}} * \frac{1\ \text{mole}}{6.022 * 10^{23}}$$

Based on these calculations, the power efficiency was found to be approximately 7.8x10$^{-6}$ to 5.6x10$^{-7}$ depending whether 1 to 14 RNA phosphodiesters are cleaved per RNA/DNA duplex.

DOI: 10.1038/NNANO.2015.259

## Supplementary Movie Captions

**Supplementary Movie 1:** Representative timelapse BF video acquired at 5 s intervals for a duration of 32 min using a 20x objective. DNA-modified particles (5 μm) were hybridised to a RNA substrate surface and treated with RNase H (5 units); 25 mM Tris pH 8.0, 8 mM NaCl, 37.5 mM KCl, 1.5 mM $MgCl_2$, 10 vol % formamide, and 0.75% (g/mL) Triton X.
**Supplementary Movie 2:** High resolution timelapse videos of BF and Cy3 fluorescence channels acquired at 12 s intervals for a duration of 17 min. The images were acquired using a 100x 1.49 NA objective. DNA-modified particles (5 μm) were hybridised to a RNA substrate surface and treated with RNase H (5 units); 25 mM Tris pH 8.0, 8 mM NaCl, 37.5 mM KCl, 1.5 mM $MgCl_2$, 10 vol % formamide, and 0.75% (g/mL) Triton X.
**Supplementary Movie 3:** High resolution timelapse videos of BF and Cy3 fluorescence channels overlaid acquired at 12 s intervals for a duration of 23 min. The images were acquired using a 100x 1.49 NA objective. DNA-modified particles (5 μm) were hybridised to a RNA substrate surface and treated with RNase H (5 units); 25 mM Tris pH 8.0, 8 mM NaCl, 37.5 mM KCl, 1.5 mM $MgCl_2$, 10 vol % formamide, and 0.75% (g/mL) Triton X.
**Supplementary Movie 4:** Movie showing an example particle from the multivalent stochastic simulation. Bound sites (blue) form randomly and instantaneously, subject to the geometric co that no two bound site are separated by more than s = 10 lattice spacings, equivalent to the path width (380 nm). Unbinding events occur stochastically, leaving hydrolyzed sites (red) that cannot be visited again. Bound times are drawn from an exponential distribution with mean 1/k, where k = 10/min. The simulation begins with the particle fully bound and ends when the particle traps itself. Note that while frames advance uniformly with each unbinding event, time advances stochastically (lower right).
**Supplementary Movie 5:** Timelapse BF video acquired at 5 s intervals for a duration of 30 min using a 20x objective. DNA-modified particles (5 μm) were hybridised to a RNA substrate surface, **subsequently blocked with a complementary strand** to prevent rolling motion, and treated with RNase H (5 units); 25 mM Tris pH 8.0, 8 mM NaCl, 37.5 mM KCl, 1.5 mM $MgCl_2$, 10 vol % formamide, and 0.75% (g/mL) Triton X.
**Supplementary Movie 6:** Timelapse BF video acquired at 5 s intervals for a duration of 8 min using a 20x objective. DNA-modified particles (5 μm) were hybridised to a RNA substrate surface and treated with RNase H (5 units); 25 mM Tris pH 8.0, 8 mM NaCl, **150 mM KCl**, 1.5 mM $MgCl_2$, 10 vol % formamide, and 0.75% (g/mL) Triton X.
**Supplementary Movie 7:** Timelapse BF video acquired at 5 s intervals for a duration of 30 min using a 20x objective. DNA-modified particles (5 μm) were hybridised to a RNA substrate surface and treated with RNase H (5 units); **25 mM Tris pH 7.5**, 8 mM NaCl, 37.5 mM KCl, 1.5 mM $MgCl_2$, 10 vol % formamide, and 0.75% (g/mL) Triton X.
**Supplementary Movie 8:** Representative Timelapse BF video acquired at 5 s intervals for a duration of 30 min using a 20x objective. DNA-modified particles (5 μm) were hybridised to a RNA substrate surface and treated with RNase H (5 units); **25 mM Tris pH 7.0**, 8 mM NaCl, 37.5 mM KCl, 1.5 mM $MgCl_2$, 10 vol % formamide, and 0.75% (g/mL) Triton X.
**Supplementary Movie 9:** Representative timelapse BF video and trajectory of single particle with self-avoiding motion that periodically becomes stalled due to entrapment. The video was acquired at 5 s intervals for a duration of 30 min using a 20x objective. DNA-modified particles (5 μm) were hybridised to a RNA substrate surface and treated with RNase H (5 units); 25 mM Tris pH 8.0, 8 mM NaCl, 37.5 mM KCl, 1.5 mM $MgCl_2$, 10 vol % formamide, and 0.75% (g/mL) Triton X.
**Supplementary Movie 10:** Representative timelapse BF video acquired at 5 s intervals for a duration of 16.75 min using a 100x objective. DNA-modified particles (500 nm) were hybridised to a RNA substrate surface and treated with RNase H (5 units); 25 mM Tris pH 8.0, 8 mM NaCl, 37.5 mM KCl, 1.5 mM $MgCl_2$, 10 vol % formamide, and 0.75% (g/mL) Triton X.

**Supplementary Movie 11:** Representative timelapse BF video acquired at 5 s intervals for a duration of 30 min using a 100x objective. DNA-modified particles (500 nm) were hybridised to a RNA substrate surface and treated with RNase H (5 units); 25 mM Tris pH 8.0, 8 mM NaCl, 75 mM KCl, 3 mM $MgCl_2$, 10 vol % formamide, and 0.75% (g/mL) Triton X.
**Supplementary Movie 12:** High-resolution timelapse BF and Cy3 fluorescence videos acquired at 20 s intervals for a duration of 1 hr using a 100x 1.49 NA objective. DNA-modified particles (5 μm) were hybridised to a **micro-patterned RNA substrate surface** and treated with RNase H (5 units); 25 mM Tris pH 8.0, 8 mM NaCl, **150 mM KCl**, 1.5 mM $MgCl_2$, 10 vol % formamide, and 0.75% (g/mL) Triton X.
**Supplementary Movie 13 and 14:** Representative BF and Cy3 fluorescence videos of **DNA-modified particle dimers** that were hybridised to a RNA substrate surface and treated with RNase H (5 units); 25 mM Tris pH 8.0, 8 mM NaCl, 37.5 mM KCl, 1.5 mM $MgCl_2$, 10 vol % formamide, and 0.75% (g/mL) Triton X. Images were collected every 12 s for 7 and 16 min durations, respectively, using a 1.49 NA 100x objective.

**Any Additional Author notes:** K.Y. conducted all experiments and analysis, A.M. performed simulations and theoretical validation, S.V. helped in data analysis and validation of theoretical model, Y.Z. helped with particle functionalization, Y.L. collected SIM data, M.F. assisted in preliminary SNP detection, K.S. and K.Y. wrote the manuscript with input from A.M. and E.R.W. K.S. oversaw all aspects of the work, E.R.W. supervised and discussed experiments with S.V.


1. Peterson, A.W., Heaton, R.J. & Georgiadis, R.M. *Nucleic Acids Res* **29**, 5163-5168 (2001).
2. Yan, L., Zhao, X.M. & Whitesides, G.M. *J Am Chem Soc* **120**, 6179-6180 (1998).
3. Johnson, K.A. & Goody, R.S. *Biochemistry-Us* **50**, 8264-8269 (2011).
4. Sbalzarini, I.F. & Koumoutsakos, P. *J Struct Biol* **151**, 182-195 (2005).
5. Domb, C., Gillis, J. & Wilmers, G. *P Phys Soc Lond* **85**, 625-& (1965).
6. Bastock, J.A., Webb, M. & Grasby, J.A. *J Mol Biol* **368**, 421-433 (2007).
7. Kuijk, A., van Blaaderen, A. & Imhof, A. *Journal of the American Chemical Society* **133**, 2346-2349 (2011).
8. Asenath-Smith, E. & Chen, W. *Langmuir* **24**, 12405-12409 (2008).
9. Slade, G. *Math Intell* **16**, 29-35 (1994).
10. Amit, D.J., Parisi, G. & Peliti, L. *Phys Rev B* **27**, 1635-1645 (1983).
11. Obukhov, S.P. & Peliti, L. *J Phys a-Math Gen* **16**, L147-L151 (1983).
12. Wang, W., Chiang, T.Y., Velegol, D. & Mallouk, T.E. *Journal of the American Chemical Society* **135**, 10557-10565 (2013).
13. Sponer, J. et al. *Physical Chemistry Chemical Physics* **14**, 15257-15277 (2012).